EUROPEAN ORGANISATION FOR NUCLEAR RESEARCH

CERN-EP/2004-XXX
25 March 2004

Measurement of the running of the QED coupling in small angle Bhabha scattering at LEP

OPAL Collaboration

Abstract

The running of the effective QED coupling $\alpha(t)$ is measured for spacelike momentum transfer $1.8 \leq -t \leq 6.0$ GeV^2 from the angular dependence of small angle Bhabha scattering by the OPAL detector at LEP. In an almost ideal QED framework, with very favourable experimental conditions and a precise experimental setup, we obtain the strongest direct evidence up to date, with a significance above 5 σ. We also report the first clear experimental evidence for the hadronic contribution to the running, with a significance of about 3 σ.

Draft 1.0

Authors:
G. Abbiendi, P. Guenther, M. Kobel

Editorial Board:
C. Hawkes, R. Kellogg, K. Nagai, D. Strom

Please send comments by Friday 9th April 2003 to:
abbiendi@bo.infn.it, guenther@physik.uni-bonn.de, mkobel@physik.uni-bonn.de

1 Introduction

The electromagnetic coupling constant is a basic parameter of the Standard Model, known to 4×10^{-9} [1]. In QED the coupling becomes effective or *running* with the scale of momentum transfer due to vacuum polarization. This is due to virtual lepton or quark loops. Their contribution increases the effective electric charge at increasing momentum transfer. This can be understood as an effect of screening of a bare electric charge which is probed at smaller and smaller distance. The effective QED coupling is generally expressed as:

$$\alpha(Q^2) = \frac{\alpha_0}{1 - \Delta\alpha(Q^2)} \tag{1}$$

where $\alpha_0 = \alpha(Q^2 = 0) \simeq 1/137.036$ is the fine structure constant. Whereas the leptonic contributions are calculable to very high accuracy, the hadronic ones are more problematic as they involve quark masses and hadronic physics at low momentum scales. The hadronic contribution is traditionally determined from a dispersion integral over a parameterization of the measured annihilation cross section of $e^+e^- \rightarrow$ *hadrons*, supplemented with perturbative QCD above resonances [2, 3]. The main difficulty of this approach comes from the integration of experimental data in the region of hadronic resonances, which in turn gives the dominant uncertainty on $\Delta\alpha$ for positive (*timelike*) Q^2. The effective QED coupling $\alpha(Q^2)$ is an essential ingredient for many precision physics predictions. Its uncertainty is still one of the dominant ones in the electroweak fits constraining the Higgs mass [4]. There are also many evaluations which are more theory-driven, extending the application of perturbative QCD down to 2 GeV or so (see for example the references in [4]). An alternative approach was put forward to use the Adler function [5] and perturbative QCD in the negative Q^2 (*spacelike*) region [6], where $\Delta\alpha$ is a smooth function.

Until now there have been only a few direct observations of the running of the QED coupling [7, 8, 9, 10]. Most of these analyses involve measurements of cross sections and their ratios and obtain values of $\alpha(Q^2)$ which are found to deviate from α_0 or from the assumed value of the coupling at some initial scale. Theoretical uncertainties on the predicted absolute cross sections as well as experimental scale errors can hurt such determinations or reduce their significance. The s-channel results from the TOPAZ [7] and the OPAL [8] experiments were based on e^+e^-annihilations to leptonic final states. Far enough from the Z resonance these processes are dominated by single photon exchange, although they substantially involve the full electroweak theory. Large angle Bhabha scattering has been studied by the VENUS [9] and L3 [10] experiments to measure the running in the spacelike region. In this case both s- and t-channel γ-exchange diagrams are important and the effective QED coupling appears as a function of s or t respectively. Moreover weak contributions of Z-exchange interference are also sizeable.

In this paper we measure the running of α in the spacelike region, by studying the angular dependence of the small angle Bhabha scattering. The spectrum is modified by the running coupling which appears as $\alpha^2(t)$ and the square momentum transfer t is simply related to the polar scattering angle. We use the small angular region accepted for the luminosity measurement, which approximately corresponds to $2 \leq -t \leq 6$ GeV^2 at centre-of-mass energy about the Z resonance peak. At such t scale the average $\Delta\alpha$ is about 2%. The counting rate of small angle Bhabha events is used to determine the integrated luminosity, so that we cannot do an absolute measurement of $\alpha(t)$, rather we will look only at the shape. This is affected by the expected variation of the coupling throughout the acceptance, which is about 0.5%, leading

to an observable effect of about 1%. An interesting property of such low $|t|$ region is that, although the absolute $\Delta\alpha$ value is dominated by the leptonic contributions, the variation of the hadronic contribution is predicted to be three times faster, resulting in similar contributions to the variation of the coupling. There has been only one previous attempt to test directly the momentum transfer dependence of α in a way free of normalization errors by the L3 collaboration [10]. To date there exists no direct experimental evidence for the hadronic contribution to the running.

The small angle Bhabha scattering appears as an ideal place for a direct measurement of the running of $\alpha(Q^2)$ in a single experiment. This has been pointed out also recently [11]. Among the advantages are the very high available statistics and the purity of the data sample. In this work a crucial part has the very high precision in measuring the scattering angle which was possible by the OPAL Silicon-Tungsten (SiW) luminometer [12]. Not less important is the cleanliness of the measurement from a theoretical point of view. Small angle Bhabha scattering is strongly dominated by single-photon t-channel exchange, while s-channel photon exchange is practically negligible. It is currently exactly calculable up to the leading $\mathcal{O}(\alpha^2)$ terms in the QED photonic corrections (herein indicated as $\mathcal{O}(\alpha^2 L^2)$, where $L = ln(|t|/m_e^2) - 1$ is the big logarithm). Many existing calculations were described in [13] and there were also widely cross-checked mainly to reduce the theoretical error on the determination of the luminosity at LEP1. Higher order terms are partially accounted through exponentiation. Many of these calculations are available in the convenient form of Monte Carlo programs and have been also extensively checked by the LEP experiments. There exists also a calculation accurate to the subleading $\mathcal{O}(\alpha^2)$ terms [14]. Corrections for Z interference are very small and well known, so that small angle Bhabha scattering is basically a pure QED process. A comparison of data with such precise calculations can determine the value of the effective QED coupling in the most precise way without relying on the correctness of the SU(2)×U(1) electroweak model.

The paper is organized in this way: in section 2 we explain the analysis method, the detector and its Monte Carlo simulation is briefly described in section 3 and the event selection in section 4. The procedure to correct the data distributions is explained in section 5. The fit results including only statistical errors are given in section 6, while the systematic errors are described in detail in section 7. The theoretical uncertainties are discussed in section 8. The results are finally given in section 9, and a conclusive summary in section 10.

2 Analysis method

The Bhabha differential cross section can be written in the following form for small scattering angle:

$$\frac{d\sigma}{dt} = \frac{d\sigma^{(0)}}{dt}\left(\frac{\alpha(t)}{\alpha_0}\right)^2 (1+\epsilon)\,(1+\delta_\gamma) + \delta_Z \tag{2}$$

where:

$$\frac{d\sigma^{(0)}}{dt} = \frac{4\pi\alpha_0^2}{t^2} \tag{3}$$

is the Born term for t-channel single photon exchange, α_0 is the fine structure constant, $\alpha(t)$ is the effective coupling at the momentum transfer scale t. Here ϵ represents the radiative corrections to the Born cross section, δ_γ the contribution of s-channel photon exchange and

δ_Z the contribution of Z exchange. The contributions of δ_γ and δ_Z are much smaller than those of ϵ and the vacuum polarization. Therefore with a precise knowledge of the radiative corrections (ϵ term) one can determine the effective coupling $\alpha(t)$ by measuring the differential cross section. Actually the form of equation (2) is an approximation as the δ_γ term is not really factorized with the effective coupling $\alpha^2(t)$. In fact the s-channel amplitude has coupling $\alpha(s)$. The practical validity is a consequence of the smallness of the δ_γ term, which could even be neglected.

The counting rate of Bhabha events in the SiW luminometers is used to determine the integrated luminosity, so that we cannot do an absolute measurement of $\alpha(t)$, unless an independent determination of the luminosity were available. Instead, the structure of the cross section as written in (2) easily allows to determine the variation of $\alpha(t)$ over the accessible t range. In fact the vacuum polarization gives the term $(\alpha(t)/\alpha_0)^2$, factorized with the dominant piece of the cross section. At the leading order the variable t is simply related to the scattering angle:

$$t = -s\,\frac{1-cos\,\theta}{2} \approx -\frac{s\theta^2}{4} \tag{4}$$

Photon radiation (in particolar Initial State Radiation) smears this correspondence. The event selection that we will be using, described in section 4, has been carefully studied to reduce the impact of radiative events. In particular the energy cuts and the acollinearity cut are very effective. As a result the event sample is strongly dominated by two cluster configurations, with almost full energy back-to-back scattered e^+ and e^-. For such selection the relation (4) is well approximated. The polar scattering angle θ is measured from the radial position R of the scattered e^+ and e^- at reference planes located within the SiW luminometers, at a distance z from the interaction point:

$$\theta = atan(R/z) \tag{5}$$

We use the BHLUMI [15] Monte Carlo generator for small angle Bhabha scattering. It is a multiphoton exponentiated generator accurate up to the leading logarithmic $\mathcal{O}(\alpha^2)$ terms. Higher order photonic contributions are partially included by virtue of the exponentiation. The generated events contain always the scattered electron and positron plus an arbitrary number of (non-collinear) photons. Small contributions from s-channel photon exchange and Z interference are also included. Corrections due to vacuum polarization are implemented with a few choices for the parameterization of the hadronic term [2, 16]. We used the option to generate weighted events, such that we could access all the available intermediate weights which compose the final complete cross section event by event. In particular we could also modify the parameterization of the vacuum polarization or set $\alpha(t) \equiv \alpha_0$ to assume a fixed coupling α_0.

We will compare the radial distribution of the data (and hence the t-spectrum) with the predictions of the BHLUMI Monte Carlo, to determine the running of α within the accepted region. We followed two equivalent methods:

- We calculated the ratios of data and Monte Carlo events in each bin. The Monte Carlo was modified by setting the coupling to the constant value $\alpha(t) \equiv \alpha_0$. Then:

$$R(t) = \frac{N_{data}}{N_{MC}} \propto \left(\frac{1}{1-\Delta\alpha(t)}\right)^2 \tag{6}$$

The dominant dependence of $\Delta\alpha(t)$ expected from theory is logarithmic. However within the kinematic region of this analysis it may be approximated with a straight line. There is no statistical sensitivity to deviations from a linear behaviour of the running. So we fitted the ratios as:

$$R(t) = a + b|t| \tag{7}$$

The b slope represents the full observable effect of the running of $\alpha(t)$, both the leptonic and the hadronic component. It is related to the variation of the coupling by:

$$b = 2\frac{\Delta\alpha(t_2) - \Delta\alpha(t_1)}{|t_2| - |t_1|} = \frac{2}{|t_2| - |t_1|}\frac{\alpha^{-1}(t_2) - \alpha^{-1}(t_1)}{\alpha_0^{-1}} \tag{8}$$

where t_1 and t_2 correspond to the acceptance limits.

- The hadronic contribution to the vacuum polarization is included in the Monte Carlo with the parameterization [16] of the form :

$$\Delta\alpha_{had} = A + B\ ln\ (1 + C\ |t|) \tag{9}$$

The coefficients A, B and C have different values in intervals of $|t|$ which depend on the detailed method of extraction of the parameterization. We fixed A and C to their values at the average $|t|$ of our data sample, leaving B as a free parameter. In this case the leptonic contribution to the vacuum polarization $\Delta\alpha_{lep}$ was kept at the calculated value.

The effective slope defined in (7) is slightly variable for the different data samples, as their average centre-of-mass energy varies. To combine the results we can practically redefine b in (7) as:

$$b = b^*\frac{\Delta t^*}{\Delta t} \tag{10}$$

where Δt is the actual energy-dependent t range, Δt^* corresponds to a reference centre-of-mass energy $\sqrt{s} = 91.1$ GeV, and then fit for b^*. With the acceptance cuts specified in section 4 the reference t range is: $t_1^* = -1.78$ GeV^2, $t_2^* = -5.96$ GeV^2, $\Delta t^* = |t_2^*| - |t_1^*| = 4.18$ GeV^2.

3 Detector, data samples and Monte Carlo simulation

The OPAL detector and trigger have been described in detail elsewhere [17]. In particular this analysis is based on the silicon-tungsten luminometer (SiW), which was used to determine the luminosity from the counting rate of accepted Bhabha events, starting from 1993. The SiW was designed to improve the precision of the luminosity measurement to better than 1 per mille. In fact it achieved a fractional experimental systematic error of 3.4×10^{-4}. The detector and the luminosity measurement are extensively described in [12]. Here we only review briefly the detector aspects relevant for this analysis.

The OPAL SiW luminometer consisted of 2 identical cylindrical calorimeters, encircling the beam pipe simmetrically at about ± 2.5 m from the interaction point. Each calorimeter is a stack of 19 silicon layers interleaved with 18 tungsten plates, with a sensitive depth of 14 cm, representing 22 radiation lenghts (X_0). The first 14 tungsten plates are each 1 X_0 thick, while

the last 4 are each 2 X_0 thick. The sensitive area fully covers radii between 6.2 and 14.2 cm from the beam axis. Each detector layer is segmented with $R-\phi$ geometry in a 32×32 pad array. The pad size is 2.5 mm radially and 11.25 degrees in azimuth. In total the whole luminometer had 38,912 readout channels corresponding to the individual silicon pads. The calibration was studied with electrical pulses generated both on the readout chips and on the front-end boards, as well as with ionization signals generated in the silicon using test beams and laboratory sources. Overall pad-to-pad gain variations were within 1%.

We use the data samples collected in 1993-95 at energies close to the Z resonance peak. In total they amount to 101 pb^{-1} of OPAL data.

For the LEP2 data-taking started in 1996 the detector configuration changed, with the installation of tungsten shields designed to protect the inner tracking detectors from synchrotron radiation. These introduced about 50 radiation lengths of material in front of the calorimeters between 26 and 33 mrad from the beam axis, thus reducing the useful acceptance of the detector at the lower polar angle limit. Moreover the new fiducial acceptance cut fell right in the middle of the previous acceptance, where the preshowering material was maximum. For these reasons we have limited this analysis to the LEP1 data samples.

The OPAL SiW detector simulation does not rely on a detailed physical simulation of electromagnetic showers in the detector. Instead it is based on a parameterization of the detector response obtained from the data [12]. This approach gives a much more reliable description of the tails of the detector response functions, which are primarily due to extreme fluctuations in shower development, than we could obtain using any existing program which attempts to simulate the basic interactions of electrons and photons in matter. The measured LEP beam size and divergence, as well as the measured offset and tilt of the beam with respect to the calorimeters are also incorporated in this simulation. The Monte Carlo simulation is used to correct the acceptance for the effects of the detector energy response, the coordinate resolution and LEP beam parameters. The data are divided in 9 subsamples according to the average centre-of-mass energy and the values of the beam parameters, which slightly varied. For each subsample we generated an independent sample of BHLUMI events subjected to detector simulation with corresponding setting of the parameters. The statistics were always at least 10 times those of the corresponding data set.

There are other acceptance corrections which are not accounted by the Monte Carlo simulation, but rather applied directly to data. These include the trigger efficiency, accidental background, detector metrology and most importantly biases in the reconstructed radial coordinate. The latter is crucial for this analysis and will be discussed in section 5.

4 Event selection

The event selection criteria can be classified into *isolation* cuts, which isolate a sample of pure Bhabha scattering events from the off-momentum background, and acceptance defining, or *definition* cuts. The isolation cuts are used to define a fiducial set of events which lie within the good acceptance of both calorimeters and are essentially background free. The definition cuts then select subsets of events from within the fiducial sample. Showers generated by incident electrons and photons are recognized as clusters in the calorimeters and their energies and

coordinates determined. The fine segmentation of the detectors allows incident particles with separations greater than 1 cm to be individually reconstructed with good efficiency.

The coordinate system used throughout this paper is cylindrical, with the z-axis pointing along the direction of the electron beam, passing through the centers of the two calorimeter bores. The origin of the azimuthal coordinate, ϕ, is in the horizontal plane, towards the inside of the LEP ring. All radial coordinate measurements are projected to reference planes at a distance of ± 246.0225 cm from the nominal intersection point. These reference planes correspond to the nominal position of the silicon layers 7 X_0 deep in the two calorimeters.

The *isolation* cuts consist of the following requirements, imposed on (R_R,ϕ_R) and (R_L,ϕ_L), the radial and azimuthal coordinates of the highest energy cluster associated with the Bhabha event, in each of the right and left calorimeters, and on E_R and E_L, the total fiducial energy deposited by the Bhabha event in each of the two calorimeters, explicitly including the energy of radiated photons:

- Loose radial cut, right (left)
$$6.7 \text{ cm} < R_R < 13.7 \text{ cm}$$
$$(6.7 \text{ cm} < R_L < 13.7 \text{ cm})$$
- Acoplanarity cut
$$||\phi_R - \phi_L| - \pi| < 200 \text{ mrad}$$
- Acollinearity cut
$$|R_R - R_L| < 2.5 \text{ cm}$$
- Minimum energy cut, right (left)
$$E_R > 0.5 \cdot E_{beam}$$
$$(E_L > 0.5 \cdot E_{beam})$$
- Average energy cut
$$(E_R + E_L)/2 > 0.75 \cdot E_{beam}$$

Note that by defining the energy cuts relative to the beam energy, E_{beam}, the selection efficiency is largely independent of $\sqrt{s}$.

The acollinearity cut (which corresponds to approximately 10.4 mrad) is introduced in order to ensure that the acceptance for single radiative events is effectively determined geometrically and not by the explicit energy cuts.

The isolation cuts accept events in which the radial coordinate, in both the Right and the Left side, is more than two pad width (0.5 cm) away from the edge of the sensitive area of the detector. The *definition* cuts, based solely on the reconstructed radial positions (R_R, R_L) of the two highest energy clusters, then require the radial position on either side to be within two extra pads towards the inside of the acceptance. For the correction procedure explained in section 5 we refer to one specified silicon layer, which can be varied with some freedom. The Right and Left *definition* cuts are chosen so as to correspond closely to radial pad boundaries in the same detector layer. When the chosen layer is the reference one at 7 X_0, the definition cuts are:

- Right side
$$7.2 \text{ cm} < R_R < 13.2 \text{ cm}$$
- Left side
$$7.2 \text{ cm} < R_L < 13.2 \text{ cm}$$

Expressed in terms of polar angles, these cuts correspond to 29.257 and 53.602 mrad. When alternative layers are chosen the acceptance cuts are projected to the layer at 7 X_0. For

example when using the layer at 4 X_0, R_{min} = 7.25842 cm and R_{max} = 13.30710 cm. The radial distributions after the isolation cuts are shown in Fig. 1 for the complete LEP1 statistics and compared to Monte Carlo distributions normalized to the same number of events. The agreement is very good, except in the central part where effects of the preshowering material are expected. Correction of the radial distributions is one of the main issues and is described in the next section.

5 Radial coordinate correction

The reconstruction of the radial coordinate is the key element to control the systematic errors to the desired accuracy. It is explained in detail in [12]. The last step is the so-called *anchoring*. This procedure was meant to correct any residual bias which could remain on the final reconstructed radius R on either side of the calorimeter at the pad boundaries defining the edges of the acceptance. For the luminosity measurement the correction affected only the total acceptance. Here we want to bin the radial distribution to determine its shape, so we need to correct for radial biases occuring at any bin edge.

The reconstruction method respects the simmetry condition that a shower which deposits equal energies on two adjacent pads in the reference layer at 7 X_0 has to be reconstructed in the mean exactly at the boundary between the pads. In reality, due to the $R-\phi$ geometry of the pads, the true position of such showers is at a smaller radius than the pad boundary. This is termed the *pad boundary bias* and depends on the lateral shower spread. The pad boundary bias has been measured in a test beam.

The test beam employed a SiW calorimeter module of 3 azimuthal wedges fully equipped in depth, and a four-plane, double-sided Si micro-strip telescope with a resolution of better than 3 μm for individual tracks. The geometry of the calorimeter pads with respect to the telescope was determined using a beam of 100 GeV muons. The muon beam was alternated with one of 45 GeV electrons.

As the radial position of the incoming particles is scanned across a radial pad boundary in a single layer, the probability for observing the largest pad signal above or below this boundary shifts rapidly, giving an image of the pad boundary as shown in Fig. 2. These plots are obtained from OPAL data taken in 1993-94 and refer to three radial pad boundaries in layer 4 X_0 of the Right calorimeter. The pad boundary images are modelled with an error function (a gaussian convoluted with a step function), where the gaussian width σ[1] is related to the resolution at the boundary and the difference between the nominal and the apparent boundary position, defined by the half-height of the step, is called the radial offset R_{off}.

At the test beam the difference in R_{off} obtained by changing from electron to muon beam was the measured pad boundary bias, which was found to follow a linear dependence increasing with σ. The fitted linear parameterization was assigned an error of 2 μm. During the OPAL running the radial position is determined by the SiW calorimeter alone, so that the width observed from the pad boundary images is an apparent one. The relation between the true σ and the apparent σ_a was also measured at the test beam and is used to convert the observed σ_a

[1] In [12] the variable w was defined differing by a numerical factor from the width: $w = \sqrt{2}\,\sigma$.

to the true σ. The uncertainty on the conversion factor from σ_a to σ has been estimated from the difference between the test beam with no additional material and with 0.84 X_0 of material in front of the detector.

In OPAL data R_{off} measures the shift of the observed pad boundary image from the nominal position of the pad boundary. Such shifts can be produced by a large number of causes: pad gain fluctuations, metrology shifts, detector malfunctions, resolution effects and preshowering. The pad boundary bias is determined by converting the apparent σ_a to the true σ and then using the test beam results to find the corresponding geometric bias. Fig. 2 shows that a gaussian resolution does not perfectly describe the tails of the distribution. To the extent that the pad boundary image maintains an odd symmetry about the apparent pad boundary, its non-gaussian behaviour does not affect the determination of R_{off} as can be seen from the close agreement of the data points and the fitted curve near the pad boundary. We have also considered a model in which the apparent pad boundary is taken as the median of the observed resolution function. The difference between the two models is assigned as a systematic error of the fit method, when it is larger than the fit statistical error, otherwise the latter is kept as estimate. A further difference of the test beam with respect to the OPAL data is that it was carried out at a radial position close to the inner acceptance cut. The geometrical bias due to $R-\phi$ pads is expected to scale as $1/R$, thus decreasing at a greater radius of pad curvature. Therefore we have scaled in this way the bias estimated by using the test beam results, but assign an additional systematic error equal to 50% of the expected bias to account for possible deviations from this behaviour.

The total net bias (also called *anchor*) δR on the position of a pad boundary is given by:

$$\delta R = R_{off} + \delta R_{R\phi} + \delta R_{res} \tag{11}$$

where R_{off} is the coordinate offset which may have positive or negative sign, $\delta R_{R\phi}$ is the pad boundary bias, always positive and δR_{res} is a small (positive) additional bias due to the resolution flow. The latter results from the steeply falling radial resolution and can be thought as a second-order effect.

From Fig. 2 one can see that the width is similar at the inner and outer radius, while it is considerably greater at the central radius. The offset R_{off} is found very small at the inner edge while it increases to $\approx 10-20$ μm at the central and the outer radius. Among other effects, the observed R_{off} is affected by fluctuations in the pad gain. We have checked these effects directly on data, by studying R_{off} as a function of the 32 azimuthal divisions of the calorimeters. We assign the size of the azimuthal variations, $(R_{off})_{RMS}/\sqrt{32}$, as a systematic error in the anchors, due to pad gain vaiations.

The anchors determined from 1993-94 data for the layers at 4 X_0 and all the pad boundaries used in the analysis are shown in Fig. 3. A similar trend is visible in the two sides, in particular the rise of the anchor from about zero at the inner edge to $20-25$ μm around $R=9$ cm. The inner error bars are the statistical errors in the fit of the pad boundary images. The full error bars include in quadrature the systematic errors from: fit method, pad gain variations, σ_a conversion, test beam parameterization and the assumed $1/R$ scaling of the pad boundary bias. The anchors determined from 1995 data have similar features although with lower statistics.

The anchors have been determined separately for 1993-94 and 1995 data, because the amount of preshowering material was different in the two sub-samples. A clear relation with the amount

and distribution of the material upstream of the calorimeters is visible from the apparent width σ_a as a function of radius, as shown in Fig. 4. The distribution of material upstream of the calorimeters was kept at a minimum especially in the crucial region of the inner acceptance cut where it amounts to 0.25 X_0. In the middle of the acceptance this material increases to about 2 X_0 due to cables and support structures of the beam pipe. The remarkable difference between the Right and Left widths in 1993-94 data is due to passage of cables from the OPAL microvertex detector. For 1995 data additional cables were installed in the Right side, which restored an almost symmetrical situation. The presence of a non-negligible amount of preshowering material in the middle of the acceptance constitutes the most delicate experimental problem, as the anchoring procedure was developed and checked at the test beam only for the almost ideal situation of a bare calorimeter or of less than 1 X_0 of preshowering material. Therefore we checked thoroughly the anchoring procedure in OPAL data before trusting its results.

The acceptance of an individual radial bin with boundaries ($R_{inn},\ R_{out}$) is corrected by introducing the anchors $\delta R_{inn},\ \delta R_{out}$ determined as in (11) in the following formula, giving the fractional correction:

$$\frac{\delta A}{A} = c_{inn}\ \delta R_{inn} - c_{out}\ \delta R_{out} \tag{12}$$

The coefficients c_{inn} and c_{out} are derived by a simple analytical calculation assuming a $1/\theta^3$ spectrum for the angular distribution and are given by:

$$c_k = \frac{\frac{1}{R_k^3}}{\frac{1}{2}\left(\frac{1}{R_{inn}^2} - \frac{1}{R_{out}^2}\right)} \qquad k = inn, out \tag{13}$$

The corrections are at most 0.5% (1%) for the Right (Left) side in 1993-94 data and 0.8% (0.7%) for the Right (Left) side in 1995 data.

The reconstructed radial coordinate can be studied by simultaneously varying the value of the radial cut in the data and in the Monte Carlo. The Monte Carlo assumes that the radial coordinate is reconstructed without bias. Thus any difference in the acceptance of the data and Monte Carlo as the inner cut is varied, beyond that expected from the finite statistics, can be attributed to biases in the radial coordinate. The relative acceptance, as a function of the value of the inner radial definition cut is shown for the Right and the Left side selection in Fig. 5 for 1993-94 data. The width of the shaded bands represents the binomial errors with respect to the reference selection 7.20 cm $\leq R \leq$ 13.20 cm. The solid points show the anchoring results for all the relevant pad boundaries in layers between 1 X_0 and 10 X_0. The estimated radial biases are converted into acceptance variations using the formula:

$$\frac{\delta A}{A} = 2\ \frac{R_{inn}^2 R_{out}^2}{R_{out}^2 - R_{inn}^2}\ \frac{\delta R}{R^3} \tag{14}$$

where $R_{inn} = 7.20$ cm, $R_{out} = 13.20$ cm and R is varied from R_{inn} to R_{out}. Since the normalization is the total acceptance, the low R points have a greater weight in the plot, as is implied by the $1/R^3$ dependence. Therefore any visible structure tends to be flattened at increasing radius.

In the plot the anchor at the inner cut $R = 7.20$ cm in layer 7 X_0 has been required to lie at zero. Each group of nearby points, marked by either circles or triangles, refer to a given pad row boundary in different layers, that is at variable depth into the calorimeters. Since all the

coordinates are projected to the reference layer 7 X_0 they are spaced by about 200 μm at the inner radius and by about 350 μm at the outer radius from one layer to the other. The arrows mark the position of a given pad row boundary in layer 7 X_0, deeper layers have a lower R and shallower layers a higher R.

As the plot shows the variation in the integrated acceptance, the most relevant thing to inspect is the slope of the acceptance variation as the radius is varied. Moreover the plot shows as reference the anchors in layer 7 X_0, as the starting value at $R = 7.20$ cm is set to zero, coincident with origin of the band. If an alternative layer is chosen the normalization should be done with respect to that point. The applicability of the method appears safe for the range of layers which give an almost flat behaviour, compatible with the shaded band. A discrepancy is apparent for the deepest layers considered ($8 - 10$ X_0), in particular for the Left side. This is most evident in the central region of acceptance, where the amount of material between the detector and the interaction point is large and the test beam measurement of the expected bias may no longer be applicable. To stay away from such problems we have selected layer 4 X_0 as the central layer for anchoring, and checked the results with alternative anchors from layer 1 X_0 to layer 7 X_0.

An amazing illustration of the anchoring capability is possible by downgrading the quality of the reconstructed radial coordinate and then determining the resulting (larger) radial biases. The last step in radial reconstruction before the anchoring procedure is a *smoothing* algorithm [12], which was implemented to remove a residual bias resulting from the variable position resolution across the pad structure of the detector. This bias has a maximum amplitude of ± 50 μm and has a periodic structure with period equal to the 2.5 mm pad width. If we repeat the game of Fig. 5, switching off the smoothing from the radial reconstruction, the result is Fig. 6. The alternative anchors track the expected acceptance variations for each of the pad rows and most of the depth range studied. Similar considerations apply here as said before. The anchoring has been further checked in the following section 7.1.

6 Fit

The fit results on the nine data sets are shown in Table 1. Each number is obtained by a linear fit as (7) on 24 points. Data have been corrected with anchors on layer 4 X_0 and only the data statistical errors are considered. The nine samples give consistent results, with χ^2 of the average of 6.5/8 for the Right side and 5.6/8 for the Left side. However the quality of some of the individual fits is not good in particular on the Left side. Considering for example the largest dataset (94 b) the χ^2 of the linear fit (7) is 27.8/22 on the Right side and 101.9/22 on the Left side. To sharpen the sensitivity to correlated systematic effects we combined the six 1993-94 distributions, the three 1995 distributions and also all the nine distributions together. We checked the quality of the fits by including also the anchoring systematic errors, discussed in the previous section. They all have been conservatively considered uncorrelated as a function of radius, except for the error of the fit method. Uncorrelated errors on the anchors actually produce anti-correlations between adjacent bins. These short range effects may deteriorate greatly the fit χ^2 even if producing small effects on the fitted slope. We have then built 24×24 covariance matrices implementing these systematic errors for radial distributions binned with 1 bin equal to 1 detector pad (2.5 mm). We checked the fit χ^2 both before and after the

anchoring correction. The results are shown in Tables 2-3 and illustrated by Figure 7 for the combination of all data. Considering that Right and Left distributions on a given data set are almost completely statistically correlated the χ^2 values should be similar. Instead we see a big χ^2 difference for the combined 1993-94 fits between the Right and Left side. This points to the presence of systematic errors. Their origin is reasonably the greater amount of preshowering material upstream of the Left side calorimeter for 1993-94 data. This will be made clearer in the next section. Allowing for the known systematic errors a good χ^2 is obtained in every case, as reported in Tables 2-3.

7 Systematic uncertainties

The systematic uncertainties are grouped in classes and summarized in Table 6.

7.1 Anchoring errors

This class includes all the uncertainties described in section 5, connected with the anchoring procedure. Their contribution on the fitted slope has been assessed by the covariance matrix described in the previous section. They have been taken as the additional quadratic contribution to the fit error on the slope and have been determined separately for the 1993-94 and 1995 data. We obtain $15(16)\times10^{-5}/GeV^2$ for the Right (Left) side in 1993-94 data and $18(21)\times10^{-5}/GeV^2$ for the Right (Left) side in 1995 data.

A practical way to check these errors on data is comparing the fitted slope obtained by anchoring in different layers of the detector. In this way we can probe at least the systematic errors which are uncorrelated between different layers. These include in particular the errors due to pad gain variations which constitute one of the main component of the total error. By anchoring on layers from 1 X_0 to 6 X_0 the standard deviation of the fitted slope is $5(26) \times 10^{-5}/GeV^2$ for the Right (Left) side in 1993-94 data and $18(19) \times 10^{-5}/GeV^2$ for the Right (Left) side in 1995 data. For the Right side the rms is within the attributed systematic error, in particular comfortably less than it for the most precise 1993-94 data. Instead for the Left side we find a significantly larger rms in 1993-94 data, greater than our estimate based on the error matrix. This further confirms the presence of leftover systematic errors for the Left side data.

The choice of the preferred Si-layer used for anchoring was motivated by the results shown in Figg. 5 and 6. Now the acceptable range of layers can be quantitatively verified by studying the variation of the fit χ^2 with the anchoring layer. We checked layers from 1 X_0 to 10 X_0 by fitting the combined data samples. The resulting χ^2 of the fit is plotted in Figure 8 before and after anchoring, considering only statistical errors. It is apparent that the reference layer 7 X_0 is much worse than shallower layers. Deeper layers (8-10 X_0) are progressively worse and worse. By considering the (cleanest) 1993-94 data in the Right side the anchoring is shown to improve the χ^2 in layers $1-6$ X_0, reaching the minimum value in layer 3 X_0. Allowing also for systematic errors the χ^2 is shown in Figure 9 for the four homogeneus data classes. This shows that the layers $1-6$ X_0 are good.

7.2 Dead material

The amount of preshowering material is maximum in the middle of the accepted radial range, as it is reflected in the σ_a distribution shown in Figure 4. We have thus defined two regions:

- clean region, $R \leq 8.2$ cm and $R \geq 11.7$ cm, corresponding to the first 4 pads starting from the inner radial cut and the last 6 pads close to the outer cut;
- bad region, $8.2 < R < 11.7$ cm, corresponding to the central 14 pads.

The fitted slopes, reported in Table 4, agree in the two regions. The breakdown of the χ^2 in Table 5 makes visible that the bad χ^2 values originate from the bad region. This is particularly evident for the larger statistics 1993-94 data. In 1995 data the χ^2 values seem under control (statistics are considerably lower though) and the two sides seem equivalent.

It is natural to expect a possible extra bias in the bad region, particularly in the Left side. We have checked for it, by introducing a new parameter x in the fit, related to this assumed extra bias with two optional models:

- *Box-model*, a naive choice assuming a constant extra bias within the bad radial region and no extra bias outside of it. Here x is the constant extra bias.
- *W-model*, the extra bias δR_{extra} is assumed to follow the pattern of σ versus R:

$$\delta R_{extra} = x \frac{\sigma(R) - \sigma(R_{inn})}{\sigma_{max} - \sigma(R_{inn})} \tag{15}$$

  where R_{inn} is the inner acceptance cut (σ is minimum there) and σ_{max} is the maximum value of σ, which is reached tipically at central radius ($R \approx 10.2$ cm). So $\delta R_{extra} = x$ when $\sigma(R) = \sigma_{max}$.

No evidence for an extra bias is found in either of the two tests. We take as systematic uncertainty the statistical sensitivity of the check, quantified as the additional contribution to the error on the slope generated by the introduction of the extra bias in the fit. We obtain $10(18) \times 10^{-5}/GeV^2$ for the Right (Left) side in 1993-94 data and $27(30) \times 10^{-5}/GeV^2$ for the Right (Left) side in 1995 data. A final verification can be done by comparing the fitted slopes in the whole acceptance (Tables 2-3) and in the restricted clean region (Table 4) for each of the various cases. The differences are always within the attributed uncertainty.

Note that the estimated error for the Left side is about twice that for the Right side in 1993-94 data. This is further commented in section 7.7.

7.3 Energy

Uncertainties due to the energy response have been assessed by varying the parameters in the detector simulation within the precision they have been estimated from the data. They

include the gaussian width of the energy response function, the exponential low-energy tail, the nonlinearity and the method used to extrapolate the energy resolution to lower energies. For each change we determined the variation in the fitted slope parameter and then we took the sum in quadrature of all the variations. The dominating uncertainty is the one on the low-energy tail of the response function, which is due to events that shower very late in the detector, events not fully contained and events with electrons and positrons that scatter off upstream material. The resulting uncertainty is $5 \times 10^{-5}/\mathrm{GeV}^2$ for both the Right and the Left calorimeter.

7.4 Beam parameters

The uncertainties related to the beam parameters are calculable as simple geometric effects which modify the radial acceptance simply assuming a $1/\theta^3$ angular distribution. Here, with regard to the slope of the radial distribution, it is enough to work out the estimates by dividing the radial acceptance in only two bins. In this way one gets in general a conservative estimate, as the isolation cuts, which are neglected analytically, decrease considerably the acceptance variations induced by the beam parameters.

The transverse beam offset is measured run-by-run with a precision better than 10 μm and gives a negligible uncertainty on the fitted slope. The beam tilt is the most important effect. Its two components are determined run-by-run as the difference of the eccentricities measured by the Right and Left calorimeters on the x and y axes. The statistical accuracy on the eccentricities is $200-300$ μm for typical runs. On the nine data sets the uncertainty related to the average beam tilt contributes $1-3 \times 10^{-5}/\mathrm{GeV}^2$. These errors have been conservatively taken twice: both correlated and uncorrelated. To cover the possibility of rapid tilt variations, on a timescale shorter than an individual run, we have conservatively taken the variation corresponding to switch off completely the beam tilt. The resulting effect depends on the measured Right and Left eccentricities, so it is slightly different in the two calorimeters, since a non zero tilt angle is measured. Note that random variations in the angles of the electron and positron beams will appear as additional contribution to the beam divergence which is considered as an independent parameter. In order for the tilts to have an effect on the acceptance which is not included in the divergence correction, the trajectories of the incoming positron and electron beams must change in a correlated manner. They range from $1 \times 10^{-5}/\mathrm{GeV}^2$ for the largest sample (94-b) to $10 \times 10^{-5}/\mathrm{GeV}^2$ in the worst cases. We have taken such numbers as uncorrelated errors, with an additional common correlated systematic equal to $1 \times 10^{-5}/\mathrm{GeV}^2$.

The transverse beam size and divergence give effects similar to a radial resolution. They can be calculated by expressing the radial acceptance variation due to the resolution flow. The uncertainty due to the beam size is conservatively estimated by taking the full size of the effect: its contribution to the slope is below $1 \times 10^{-5}/\mathrm{GeV}^2$ and has been neglected. The uncertainty on the beam divergence, estimated by comparing two independent determinations, ranges from ≈ 100 μrad for 1993-94 data and ≈ 130 μrad for 1995 data. The resulting uncertainty on the slope is $1 \times 10^{-5}/\mathrm{GeV}^2$ and $2 \times 10^{-5}/\mathrm{GeV}^2$ respectively. We have taken these errors as uncorrelated but additionally a correlated term equal to 1×10^{-5} has been considered.

The longitudinal position of the beam spot has a constant effect on the radial acceptance so gives no contribution to the slope. The same holds for the longitudinal size of the beam spot.

The uncertainties estimated in this way have been checked with the results of Monte Carlo simulations where one parameter at a time can be varied. In this case the isolation cuts are included, at the price of some statistical limitation. The results are consistent.

7.5 Radial resolution

The radial resolution at pad boundaries in the clean acceptance near the inner edge of the detector has been measured at the test beam to be 130 μm. The apparent resolution at the outer edge and in the central portion of the detector, behind the bulk of the preshowering material, is degraded approximately by a factor of 2 to 2.5, according to the pattern of Figure 4. The Monte Carlo simulation includes an average radial dependence accounting for this. We conservatively assessed the uncertainty related to radial resolution by dividing the acceptance in two radial bins and calculating the full effect of the resolution flow on the slope. It amounts to $4(10) \times 10^{-5}/\mathrm{GeV}^2$ for the Right (Left) side of 1993-94 data and $7(9) \times 10^{-5}/\mathrm{GeV}^2$ for the Right (Left) side of 1995 data. The contribution of the resolution flow across the acollinearity cuts is negligible in comparison, amounting to $1 \times 10^{-5}/\mathrm{GeV}^2$ in all cases.

7.6 Acollinearity bias

The acollinearity distribution, with the selection cuts $|\Delta R| \leq 2.5$ cm, is not anchored as the radial distribution. Therefore it is subjected to biases of the order of the anchors themselves. In the worst case there could be a first order effect causing a net gain or loss of events at both the positive and the negative ΔR cut. This is conservatively estimated by considering a bias with absolute value $\Delta R_{bias} = 30$ μm, which is the maximum value reached by the anchors. In addition the smoothed radial coordinate has an inherent bias of up to 15 μm which gives another uncorrelated contribution. The sum in quadrature of both the two effects gives an uncertainty on the slope of $3 \times 10^{-5}/\mathrm{GeV}^2$.

7.7 Summary of systematic errors

We have observed significant differences between the Right and the Left side radial distributions, which are consistently understood as effects of the different amount of preshowering material for the bulk of data, taken in 1993-94. The Left side calorimeter had more dead material upstream and this is reflected in the apparent radial resolution (Figure 4) and in the plots comparing data and Monte Carlo (Figures 1, 5, 6). The χ^2 of our fits is very sensitive to any bias in data and we found that the central region behind the bulk of material in the Left side is mostly responsible for the observed bad χ^2 values. The anchoring procedure to correct radial biases has proven capable to deal with less than 2 X_0 of preshowering material which was present upstream of the Right side calorimeter, but seems insufficient for the slightly worse conditions of the Left calorimeter, with less than 1 X_0 extra material. Despite this modest difference, the data quality is visibly different. We believe that this is due to the highly non-linear behaviour of preshowering effects. The study of anchors and fit χ^2 as function of the silicon layer depth supports this interpretation.

The dominant systematic errors are the ones related to anchoring and dead material, described in sections 7.1 and 7.2. The latter was estimated to be almost twice for the Left side w.r.t. the Right side. To keep the systematic errors at the minimum we used the Right side data for the final fit, while the Left side was looked at only as a check. The difference between them is anyway quite small, $b^*_{Left} - b^*_{Right} = -22 \times 10^{-5}/\mathrm{GeV}^2$, as can be seen in Table 1. This is found to reduce to $+8 \times 10^{-5}/\mathrm{GeV}^2$ when a coarser binning is used, as for the final result.

The experimental systematic uncertainties are summarized in Table 6 for the Right side data. The quadratic sum of the correlated and uncorrelated systematic errors is about $29 \times 10^{-5}/\mathrm{GeV}^2$ for the Right side 1993-94 data and 40×10^{-5} for 1995 data. The larger error of 1995 data is due to the increased preshowering material.

The final experimental error correlation matrix (including the statistical errors) is given in Table 7. The correlations reach at most 10 %. The classification of the detailed sources of error into correlated and uncorrelated components given in Table 6 does not reveal the complete pattern of correlations embodied in the full correlation matrix. In that table the errors classified as correlated are fully correlated between all data samples, while those classified as uncorrelated are often correlated within a given year, but uncorrelated between years.

8 Theoretical uncertainties

It is very important to assess the theoretical uncertainties implied by the BHLUMI Monte Carlo. In fact a reliable determination of the running coupling constant from equation (2) needs a precise knowledge of the radiative corrections.

The theoretical uncertainty of the BHLUMI calculation of small angle Bhabha scattering has been extensively studied for the typical selections of LEP experiments. The accepted fractional theoretical error is 6.1×10^{-4} for the integrated cross section at LEP1 energy [13, 18] which was relevant for the determination of the integrated luminosity. Alternative existing calculations have been widely cross-checked with BHLUMI [13]. Moreover all the four LEP collaborations used this Monte Carlo for many years, guarantee for possible technical imperfections. Therefore the estimate of the theoretical uncertainty of BHLUMI is solid. BHLUMI does not include diagrams with extra light pairs ($e^+e^-, \mu^+\mu^-, ...$). Their contribution was calculated explicitly for the (idealized) OPAL acceptance, giving a fractional correction of $-4.4 \pm 1.4 \times 10^{-4}$ [19]. With this correction the theoretical error on the integrated luminosity was reduced to 5.4×10^{-4}, dominated by uncertainties on vacuum polarization and photonic corrections.

We have studied the uncertainty on the slope of the differential cross section in a conservative way, by degrading the precision of BHLUMI of the last perturbative order. Since BHLUMI includes completely the $\mathcal{O}(\alpha^2 L^2)$ terms we have compared it to the exact $\mathcal{O}(\alpha)$ calculation. This check has the additional advantage that within the BHLUMI package it is available the independent fixed $\mathcal{O}(\alpha)$ calculation of the former OLDBIS Monte Carlo programme [20], which is in turn based on the calculation of an independent group [21]. Thus this check covers also the technical precision. BHLUMI gives access to many intermediate weights which compose the final calculation, so that we could also check several different approximations.

We did this study by using a slightly modified version of the idealized model of the OPAL

detector, which is contained in the BHLUMI package (subroutine TRIOSIW). We generated the events within a safely enlarged angular region to protect against loss of visible events. This code was used also for the work of [13]. Smearing effects are neglected and an ideal beam is assumed. Nearby particles are combined by a clustering algorithm which has a window matched to the experimental resolution. The energy is defined by summing all the particles inside the isolation cuts on each calorimeter. The position variables R and ϕ are defined as the coordinates of the highest energy particle reconstructed on each side. On these reconstructed variables we applied all the isolation cuts listed in section 4. The differential cross section obtained at different perturbative orders is shown in Figure 10 normalized to the reference BHLUMI cross section. Here vacuum polarization, Z-exchange interference and s-channel photon interference have been switched off. The Born cross section is reduced by about $5-15$ % by radiative corrections, depending on the polar angle. Cross section at $\mathcal{O}(\alpha)$ is slightly lower than the reference but in general within 1 %, except for the upper edge of the angular acceptance where the difference is close to 2 %. The $\mathcal{O}(\alpha)_{exp}$ calculation is almost identical to the reference.

We fit the ratio of calculations at different orders and determine the b-slope, which would transfer on our fit of data. The results are shown in Figure 11 and are:

$$OLBIS[\mathcal{O}(\alpha)]/BHLUMI \Rightarrow b = -29 \pm 21 \times 10^{-5}/GeV^2$$
$$\mathcal{O}(\alpha)_{exp}/BHLUMI \Rightarrow b = +6 \pm 13 \times 10^{-5}/GeV^2$$

We take half the result of the $\mathcal{O}(\alpha)$/BHLUMI fit as a conservative estimate of the systematic error related to neglected photonic corrections ($14 \times 10^{-5}/\mathrm{GeV}^2$). The size of the window used by the cluster algorithm (on R and ϕ) has been varied over a large range to verify the stability of the result. The result of the $\mathcal{O}(\alpha)$/BHLUMI fit moves at most by $3 \times 10^{-5}/\mathrm{GeV}^2$, while the $\mathcal{O}(\alpha)_{exp}$/BHLUMI fit is unchanged. We point out that the acollinearity cut applied by our selection is very effective in reducing the importance of the photonic radiative corrections. An alternative idealized selection (similar to the ALEPH standard selection, named SICAL in [13]) without such a cut would end to a systematic error of $25 \times 10^{-5}/\mathrm{GeV}^2$ according to the same procedure.

The interference with Z exchange amplitude in the s-channel is a small correction, indicated with δ_Z in equation (2), not factorized with respect to the main contribution and the running coupling constant. It is energy dependent, vanishing at $\sqrt{s} = m_Z$ and changing sign across the Z mass. In BHLUMI it is calculated at $\mathcal{O}(\alpha)_{exp}$ with vacuum polarization correction included. Alternatively it can be obtained at the same order but without the vacuum polarization correction, at the Leading-Log level $\mathcal{O}(\alpha^0)_{exp}$ or at the Born level. We have studied the effect of uncertainties on this piece by degrading the default calculation to the Born approximation for δ_Z. We generated large samples of events at three different energy points: the Z-peak energy (set to $\sqrt{s} = 91.1$ GeV) and energies offset by 2 GeV up and down. Radiative corrections on Z interference are found to shift the fitted slope by $+31 \pm 15 \times 10^{-5}/\mathrm{GeV}^2$ at $\sqrt{s} = 89.1$ GeV and $-20 \pm 15 \times 10^{-5}/\mathrm{GeV}^2$ at $\sqrt{s} = 93.1$ GeV with respect to result obtained with the Born calculation. We have checked also the effect of the inclusion of vacuum polarization in the δ_Z term, as this subtle effect could in principle perturb the asserted cleanliness of the measurement. We find $\pm 7 \times 10^{-5}/\mathrm{GeV}^2$ for the induced shifts on the fitted slope, much less than the effect of photonic corrections. The estimated theoretical uncertainties are summarized in Table 8.

9 Results

The results are plotted in Fig. 12. Data are clearly incompatible with the hypothesis of fixed coupling and also show a steeper slope than the expected behaviour for vacuum polarization involving only leptons. The fitted linear dependence agrees well with the prediction of the standard Burkhardt-Pietrzyk parameterization [16].

The combined value of the effective slope b^* is:

$$b^* = (200 \pm 29 \pm 24) \times 10^{-5}/GeV^2 \tag{16}$$

where the first error is statistical and the second the experimental systematic. The statistical significance of the measurement is 6.8σ, which becomes 5.2σ including the systematic errors. The effective slope gives a measurement of the variation of the coupling $\alpha(t)$ by inverting equation (8):

$$\alpha^{-1}(-1.90\ GeV^2) - \alpha^{-1}(-5.27\ GeV^2) = 0.462 \pm 0.067 \pm 0.055 \tag{17}$$

This includes a very small correction of -0.007 for the bias of the method of linear fit instead of the assumed logarithmic dependence. Our result is about 1σ lower than the prediction of the Burkhardt-Pietrzyk parameterization included in BHLUMI [16] for the same t interval (which gives 0.536).

If we take from the theoretical prediction the leptonic contribution to the running, $\delta(\Delta\alpha_{lep}) = 0.001698$, which is known to a very high accuracy, we can determine the hadronic contribution as:

$$\Delta\alpha_{had}(-1.90\ GeV^2) - \Delta\alpha_{had}(-5.27\ GeV^2) = 0.00167 \pm 0.00049 \pm 0.00040 \tag{18}$$

This has a statistical significance of $3.4\,\sigma$, reduced to $2.6\,\sigma$ considering also the systematic errors. Up to date this is the most significant experimental observation of the running of the QED coupling in a single experiment and the cleanest possible when also theoretical uncertainties are properly considered.

10 Conclusions

The scale dependence of the effective QED coupling $\alpha(t)$ has been measured from the angular spectrum of small angle Bhabha scattering by using the precise OPAL Silicon-Tungsten calorimeters which were employed to determine the integrated luminosity. Despite the narrow accessible t range, the method has high sensitivity due to the very high statistics and purity of the data sample. The challenging aspect of the analysis is controlling the residual bias of the reconstructed radial coordinate of Bhabha electrons impinging the detector face to a level below ≈ 10 μm uniformly through all the acceptance. From a theoretical point of view the environment is almost ideal as of cleanliness of the measurement. In fact for this kinematic range the process is almost a pure QED one, Z interference is very small and the dominant diagram is t-channel single-photon exchange, while s-channel photon exchange is negligible. The small angle Bhabha scattering is one of the most precisely calculable processes, so there is no significant contamination from photonic radiative corrections. We tested such point in a

very conservative way and found that the radiative corrections are almost decoupled from the t-slope, at least for the OPAL selection, which strongly reduces non-collinear final states.

We determined the effective slope of the Bhabha momentum transfer distribution which is simply related to the average derivative of $\Delta\alpha$ as a function of t ($b^* \simeq 2\dot{<}\frac{\delta(\Delta\alpha)}{\delta t}>$) in the range $2 \leq -t \leq 6$ GeV^2. The observed t-spectrum agrees with the predicted behaviour of the standard Burkhardt-Pietrzyk parameterization within 1 σ.

We obtain the strongest direct evidence for the running of α_{QED} in a single experiment up to date, with significance above 5 σ. Moreover we report the first clear experimental evidence for the hadronic contribution to the running, with a significance of about 3 σ. This is one of the very few existing experimental tests of the running of $\alpha(t)$ in the spacelike region, where $\Delta\alpha$ has a smooth behaviour.

Acknowledgements

We are pleased to acknowledge useful discussions with M. Caffo and L. Trentadue.

References

[1] P. J. Mohr and B. N. Taylor, Rev. Mod. Phys. **72** (2000) 351.

[2] S. Eidelman and F. Jegerlehner, Z. Phys. C **67** (1995) 585.

[3] H. Burkhardt and B. Pietrzyk, Phys. Lett. B **513** (2001) 46.

[4] The LEP Collaborations ALEPH, DELPHI, L3 and OPAL, the LEP Electroweak Working Group and the SLD Heavy Flavour Group, CERN-EP-2003-091, hep-ex/0312023.

[5] S. L. Adler, Phys. Rev. D **10** (1974) 3714.

[6] S. Eidelman, F. Jegerlehner, A.L. Kataev, O. Veretin, Phys. Lett. B **454** (1999) 369; F. Jegerlehner, hep-ph/0308117.

[7] TOPAZ Collaboration, I. Levine *et al.*, Phys. Rev. Lett. **78** (1997) 424.

[8] OPAL Collaboration, G. Abbiendi *et al.*, CERN-EP-2003-053, submitted to Eur. Phys. J. C.

[9] VENUS Collaboration, S. Odaka *et al.*, Phys. Rev. Lett. **81** (1998) 2428.

[10] L3 Collaboration, M. Acciarri *et al.*, Phys. Lett. B **476** (2000) 40

[11] A. B. Arbuzov, D. Haidt, C. Matteuzzi, M. Paganoni and L. Trentadue, hep-ph/0402211.

[12] OPAL Collaboration, G. Abbiendi*et al.*, Eur. Phys. J. C **14** (2000) 373.

[13] S. Jadach, O. Nicrosini*et al.*, in *Physics at LEP2*, CERN 96-01, ed. G. Altarelli, T. Sjöstrand and F. Zwirner (CERN, Geneva, 1996), Vol. 2, pages 229–298.

[14] A.B. Arbuzov, V.S. Fadin, E.A. Kuraev, L.N. Lipatov, N.P. Merenkov and L. Trentadue, Nucl. Phys. **B485** (1997) 457.

[15] S. Jadach, W. Placzek, E. Richter-Was, B. F. L. Ward and Z. Was, Comput. Phys. Commun. **102** (1997) 229.

[16] H. Burkhardt and B. Pietrzyk, Phys. Lett. B **356** (1995) 398.

[17] OPAL Collaboration, K. Ahmet *et al.*, Nucl. Instrum. Meth. A **305** (1991) 275.

[18] B. F. L. Ward, S. Jadach, M. Melles and S. A. Yost, Phys. Lett. B **450** (1999) 262.

[19] G. Montagna, M. Moretti, O. Nicrosini, A. Pallavicini and F. Piccinini, Phys. Lett. B **459** (1999) 649; Nucl. Phys. B **547** (1999) 39.

[20] S. Jadach, E. Richter-Was, B. F. L. Ward and Z. Was, Comput. Phys. Commun. **70** (1992) 305.

[21] F. A. Berends and R. Kleiss, Nucl. Phys. B **228** (1983) 537.

Dataset	Right b^* slope $\times 10^{-5}/\mathrm{GeV}^2$	Left b^* slope $\times 10^{-5}/\mathrm{GeV}^2$
93 −2	$139. \pm 98.$	$94. \pm 98.$
93 pk	$211. \pm 98.$	$268. \pm 98.$
93 +2	$153. \pm 100.$	$159. \pm 100.$
94 a	$124. \pm 98.$	$58. \pm 98.$
94 b	$252. \pm 46.$	$217. \pm 46.$
94 c	$16. \pm 172.$	$105. \pm 171.$
95 −2	$247. \pm 98.$	$199. \pm 98.$
95 pk	$251. \pm 121.$	$188. \pm 121.$
95 +2	$47. \pm 98.$	$58. \pm 98.$
Average	$194. \pm 29.$	$172. \pm 29.$
χ^2/d.o.f.	6.5/8	5.6/8

Table 1: Fitted slope for each data subsample and average for the Right and the Left radial distributions. The errors are only statistical.

Dataset	Right side				
	Anchoring correction	b^* slope $\times 10^{-5}/\mathrm{GeV}^2$	χ^2_{unc} (d.o.f.=22)	χ^2_{cor} (d.o.f.=22)	
				stat.	*stat.+syst.*
1993-94	$-13. \times 10^{-5}/\mathrm{GeV}^2$	$201. \pm 33. \pm 18.$	51.8	40.8	11.2
1995	$+19. \times 10^{-5}/\mathrm{GeV}^2$	$172. \pm 60. \pm 22.$	22.3	35.1	15.9

Table 2: Results of a combined fit on homogeneus data sets for the Right radial distribution, giving the anchoring correction for the slope, the corrected slope with statistical and (anchoring) systematic error and the fit χ^2 for the uncorrected and the corrected distributions with only statistical or statistical plus systematic errors with their covariance matrix.

Dataset	Left side				
	Anchoring correction	b^* slope $\times 10^{-5}/\mathrm{GeV}^2$	χ^2_{unc} (d.o.f.=22)	χ^2_{cor} (d.o.f.=22)	
				stat.	*stat.+syst.*
1993-94	$-10. \times 10^{-5}/\mathrm{GeV}^2$	$181. \pm 33. \pm 19.$	126.4	137.1	28.4
1995	$+19. \times 10^{-5}/\mathrm{GeV}^2$	$144. \pm 60. \pm 24.$	33.4	47.7	19.5

Table 3: Results of a combined fit on homogeneus data sets for the Left radial distribution, giving the anchoring correction for the slope, the corrected slope with statistical and (anchoring) systematic error and the fit χ^2 for the uncorrected and the corrected distributions with only statistical or statistical plus systematic errors with their covariance matrix.

Dataset	Right b^* slope $\times 10^{-5}/\mathrm{GeV}^2$	Left b^* slope $\times 10^{-5}/\mathrm{GeV}^2$
1993-94 CLEAN	$195. \pm 40.$	$168. \pm 40.$
BAD	$207. \pm 76.$	$225. \pm 76.$
1995 CLEAN	$202. \pm 70.$	$149. \pm 70.$
BAD	82 ± 134	$124. \pm 134.$
All CLEAN	$196. \pm 35.$	$163. \pm 35.$
BAD	$177. \pm 66.$	$200. \pm 66.$

Table 4: Fitted slope separately for the CLEAN and the BAD radial range of acceptance, for homogeneus data sets. Both the Right and the Left side results are given. The errors are only statistical.

Dataset	Right side		Left side	
	χ^2/d.o.f.		χ^2/d.o.f.	
	stat.	*stat.+syst.*	*stat.*	*stat.+syst.*
1993-94 CLEAN	13.6 /8	5.0 /8	18.7 /8	6.5 /8
1995 CLEAN	12.5 /8	7.0 /8	4.0 /8	1.4 /8
1993-94 BAD	22.2 /12	6.3 /12	98.1 /12	21.2/12
1995 BAD	20.6 /12	8.6 /12	42.0 /12	17.1 /12

Table 5: χ^2 of the separate fits to the CLEAN and the BAD radial range of acceptance, for homogeneus data sets, for both the Right and the Left side distributions. The given values are obtained after anchoring considering only statistical errors or statistical and systematic errors with their covariance matrix.

Uncertainty	93 -2	93 pk	93 +2	94a	94b	94c	95 -2	95 pk	95 +2
Anchoring									
uncorrelated	3.	3.	3.	3.	3.	3.	6.	6.	6.
correlated	15.	15.	15.	15.	15.	15.	17.	17.	17.
Dead Material									
uncorrelated	0.	0.	0.	0.	0.	0.	0.	0.	0.
correlated	10.	10.	10.	10.	10.	10.	27.	27.	27.
Energy									
uncorrelated	0.	0.	0.	0.	0.	0.	0.	0.	0.
correlated	5.	5.	5.	5.	5.	5.	5.	5.	5.
Beam parameters									
uncorrelated	5.	9.	6.	2.	2.	4.	4.	7.	9.
correlated	2.	2.	2.	2.	2.	2.	2.	2.	2.
Radial resolution									
uncorrelated	0.	0.	0.	0.	0.	0.	0.	0.	0.
correlated	4.	4.	4.	4.	4.	4.	7.	7.	7.
Acollinearity bias									
uncorrelated	0.	0.	0.	0.	0.	0.	0.	0.	0.
correlated	3.	3.	3.	3.	3.	3.	3.	3.	3.
M.C. statistics									
uncorrelated	21.	21.	21.	38.	21.	65.	21.	21.	21.
correlated	0.	0.	0.	0.	0.	0.	0.	0.	0.
Sum									
uncorrelated	22.	23.	22.	38.	21.	65.	22.	23.	23.
correlated	19.	19.	19.	19.	19.	19.	33.	33.	33.
Total Systematic error	29.	30.	29.	43.	29.	68.	40.	40.	41.

Table 6: Summary of the systematic uncertainties on the measurement of the effective slope b^* for the nine data sets. They are given broken down into the component uncorrelated among the data sets and the correlated one. All errors are in units of $10^{-5}/\mathrm{GeV}^2$.

Sample	93 -2	93 pk	93 +2	94 a	94 b	94 c	95 -2	95 pk	95 +2
93 -2	1.00	0.04	0.04	0.04	0.07	0.02	0.05	0.05	0.05
93 pk	0.04	1.00	0.04	0.04	0.07	0.02	0.05	0.05	0.05
93 +2	0.04	0.04	1.00	0.03	0.07	0.02	0.05	0.04	0.05
94 a	0.04	0.04	0.03	1.00	0.07	0.02	0.05	0.04	0.05
94 b	0.07	0.07	0.07	0.07	1.00	0.04	0.10	0.09	0.10
94 c	0.02	0.02	0.02	0.02	0.04	1.00	0.03	0.03	0.03
95 -2	0.05	0.05	0.05	0.05	0.10	0.03	1.00	0.08	0.10
95 pk	0.05	0.05	0.04	0.04	0.09	0.03	0.08	1.00	0.08
95 +2	0.05	0.05	0.05	0.05	0.10	0.03	0.10	0.08	1.00

Table 7: The experimental correlation matrix of the nine data sets.

Error source	$\delta b \times 10^{-5}/GeV^2$		
	peak	peak - 2	peak + 2
Photonic corrections	14.	14.	14.
Z-interference	7.	16.	14.
Total	16.	21.	20.

Table 8: The estimated theoretical uncertainties on the measurement of the effective slope b^*, at centre-of-mass energies of 91.1, 89.1, 93.1 GeV.

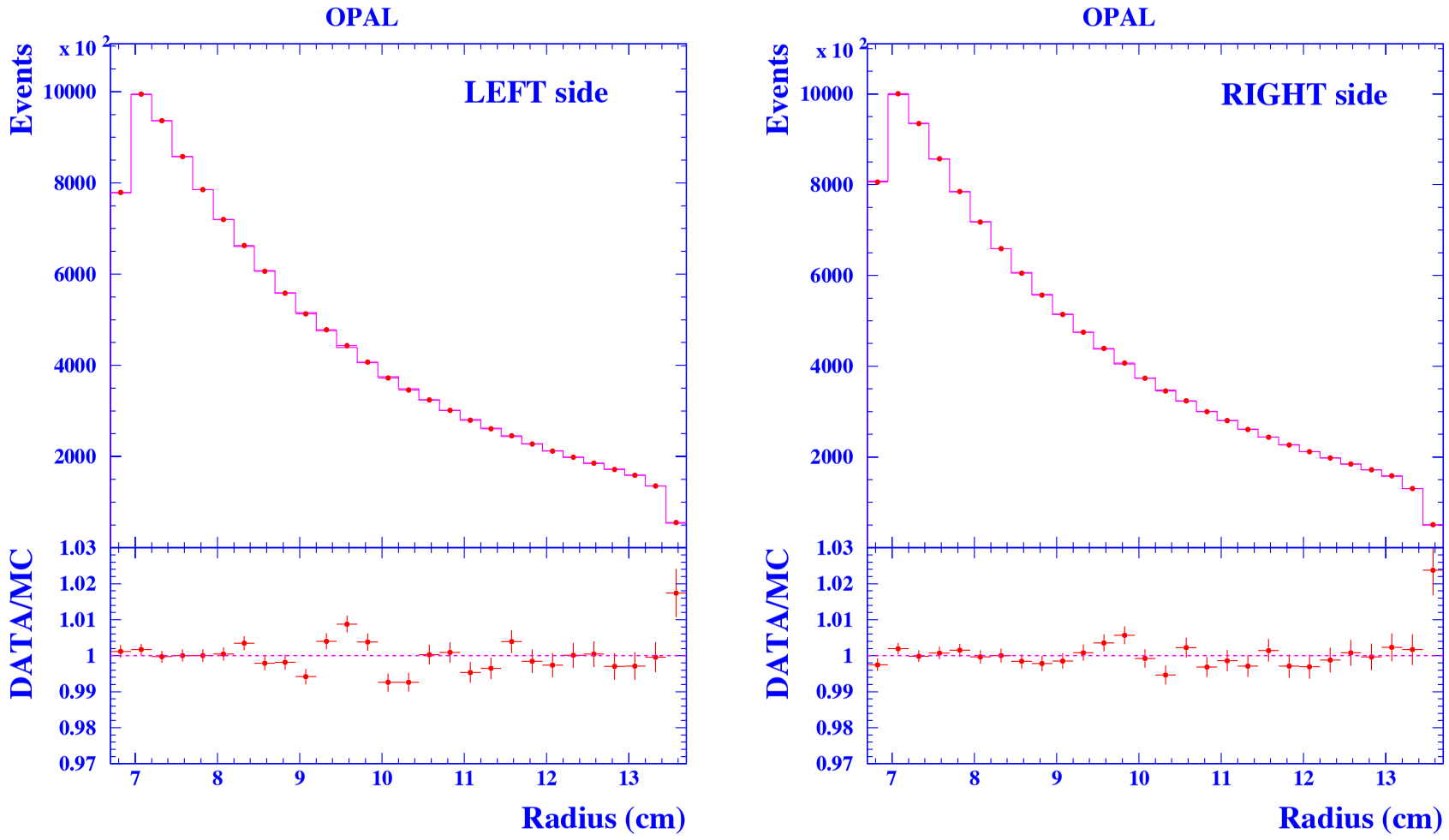

Figure 1: Radial distributions after the isolation cuts for the complete LEP1 statistics in the Right and Left calorimeters. The points show the data and the histogram the Monte Carlo predicition normalized to the same number of events. The lower plots show the ratio between data and Monte Carlo.

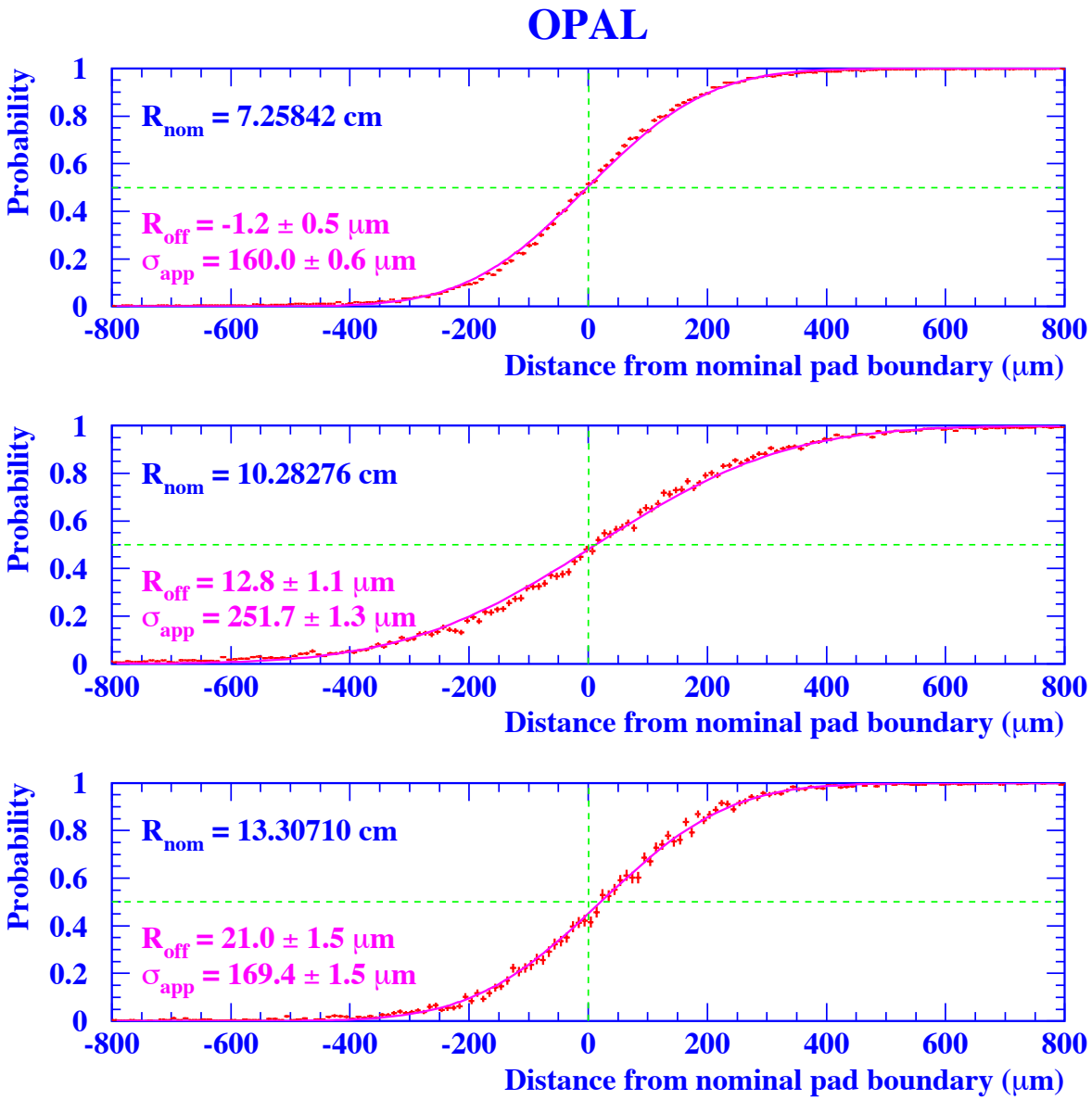

Figure 2: Pad boundary images obtained on Si-layer after 4 X_0 at three different radial positions corresponding to the inner edge, the middle portion and the outer edge of the acceptance. The solid curve shows the fitted function, whose parameters R_{off} and σ_{app} are written.

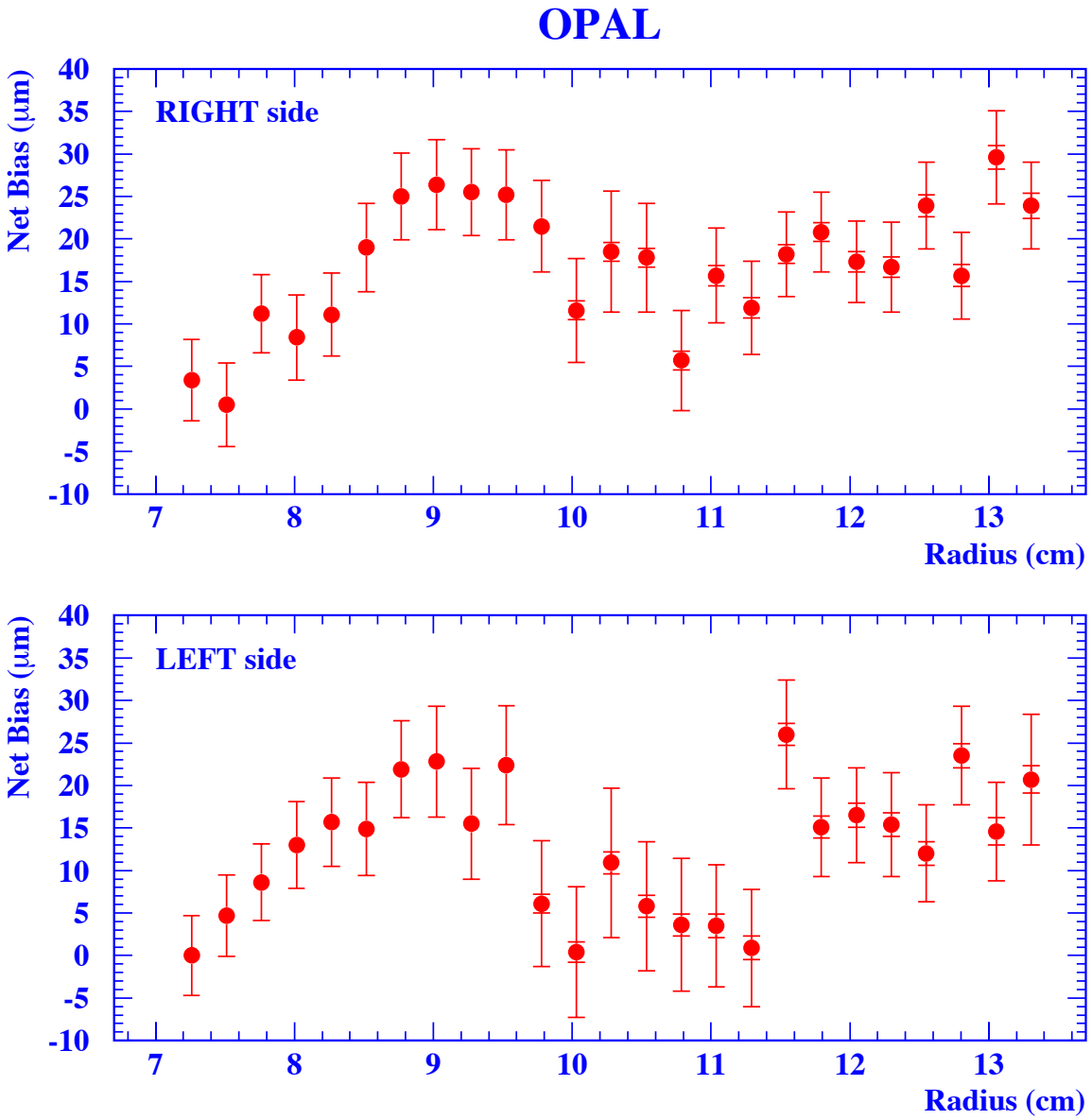

Figure 3: The total net bias (*anchor*) as a function of radius for the Right (upper plot) and the Left (bottom plot) radial coordinate determined on Si-layer after 4 X_0, for the combined 1993-94 data sample. The full error bars show the total error, the inner bars the statistical component.

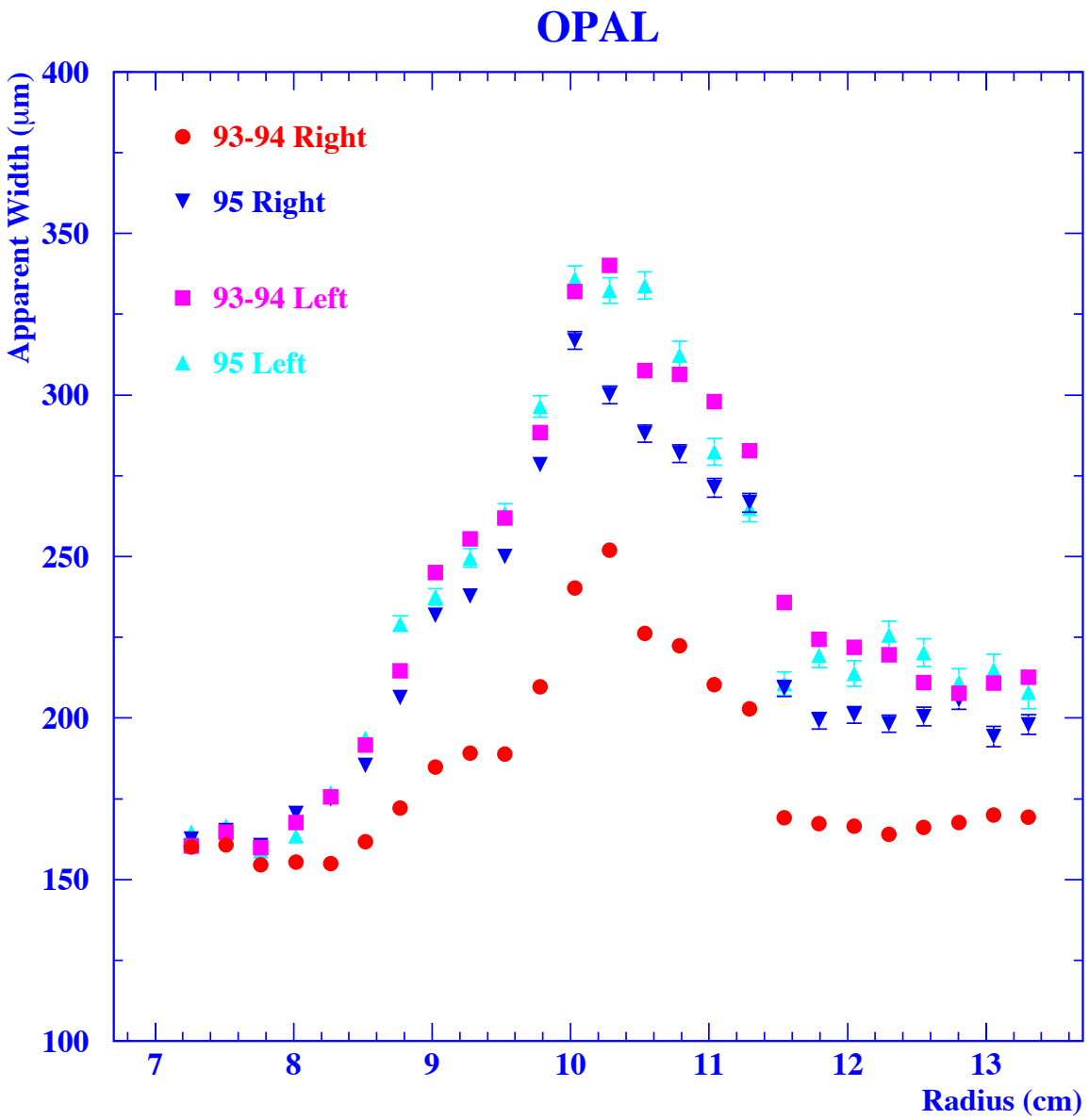

Figure 4: The apparent width as a function of radius determined from the anchoring procedure on Si-Layer after 4 X_0 for the four homogeneus data subsamples. The included errors are only statistical.

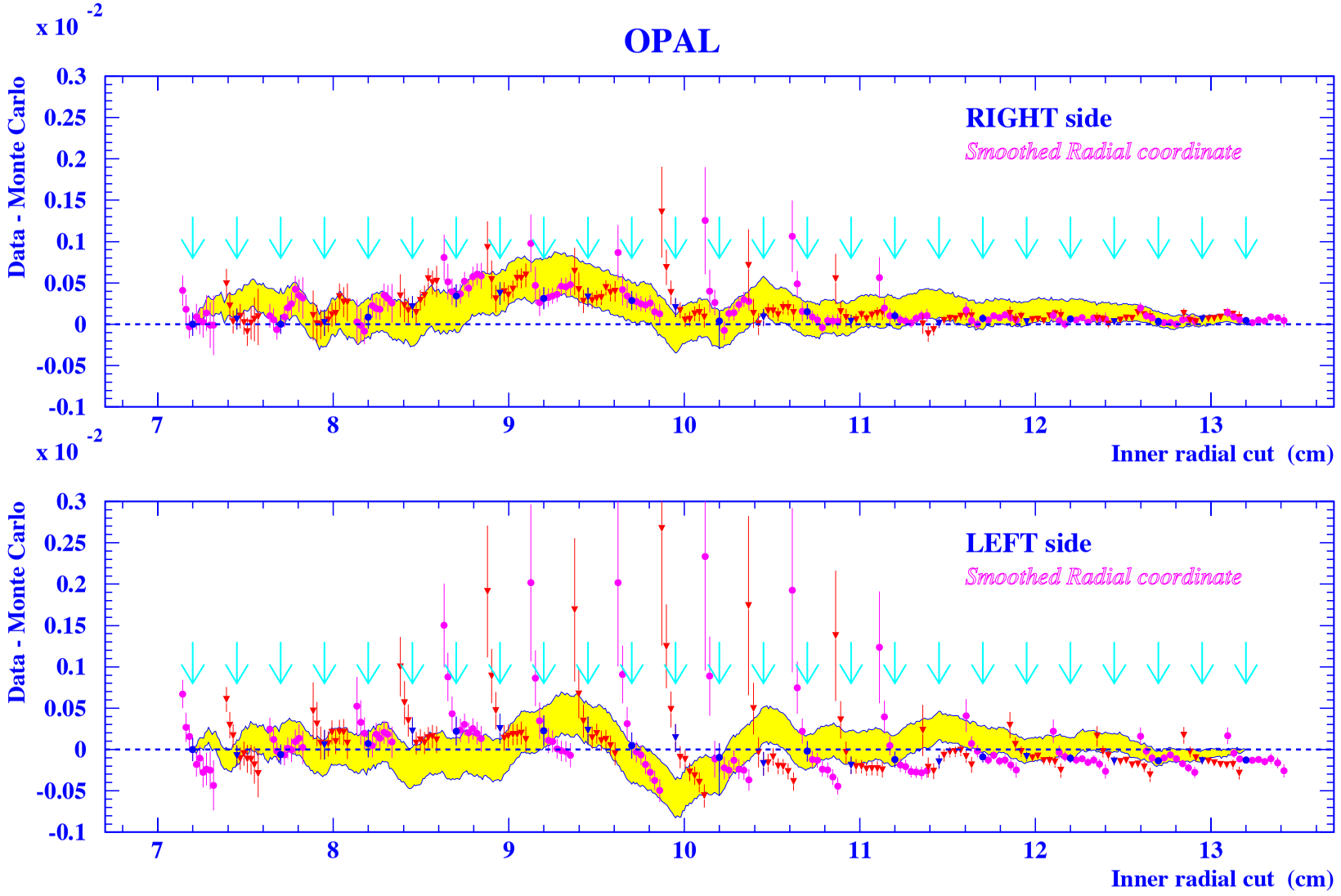

Figure 5: Study of the final reconstructed radial coordinate, including the smoothing. The shaded band shows the relative change in acceptance between data and Monte Carlo as a function of the definition cut on the inner radius for the combined 1993-94 data sample. The width of the band shows the (highly correlated) statistical errors. The solid points correspond to the coordinate bias measured by the anchoring procedure in Si-layers from 1 X_0 to 10 X_0, with the total errors shown. Here the anchor at $R = 7.2$ cm is fixed to lie at zero. The arrows show the location of the radial pad boundaries in layer 7 X_0.

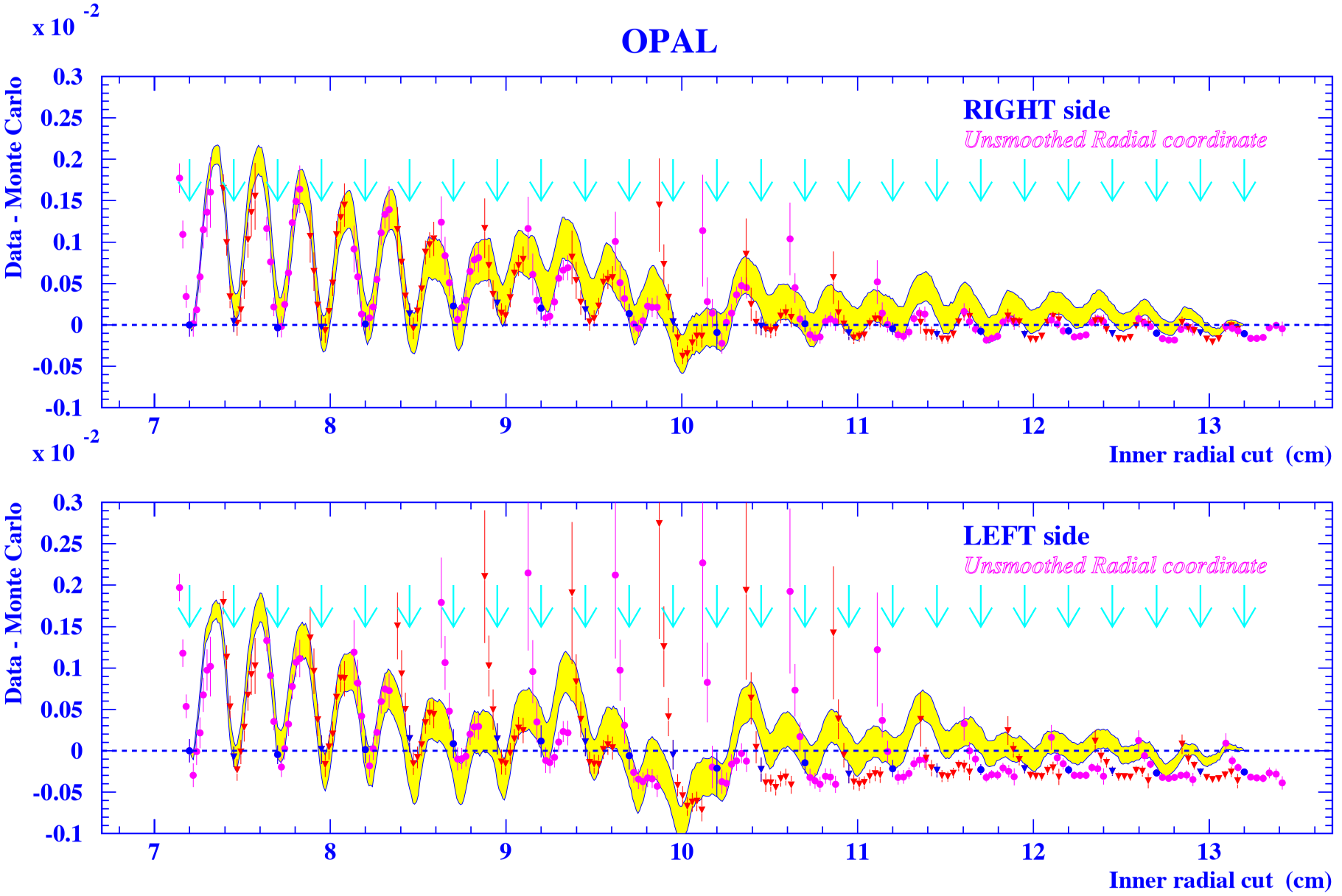

Figure 6: As in Figure 5, for the unsmoothed radial coordinate.

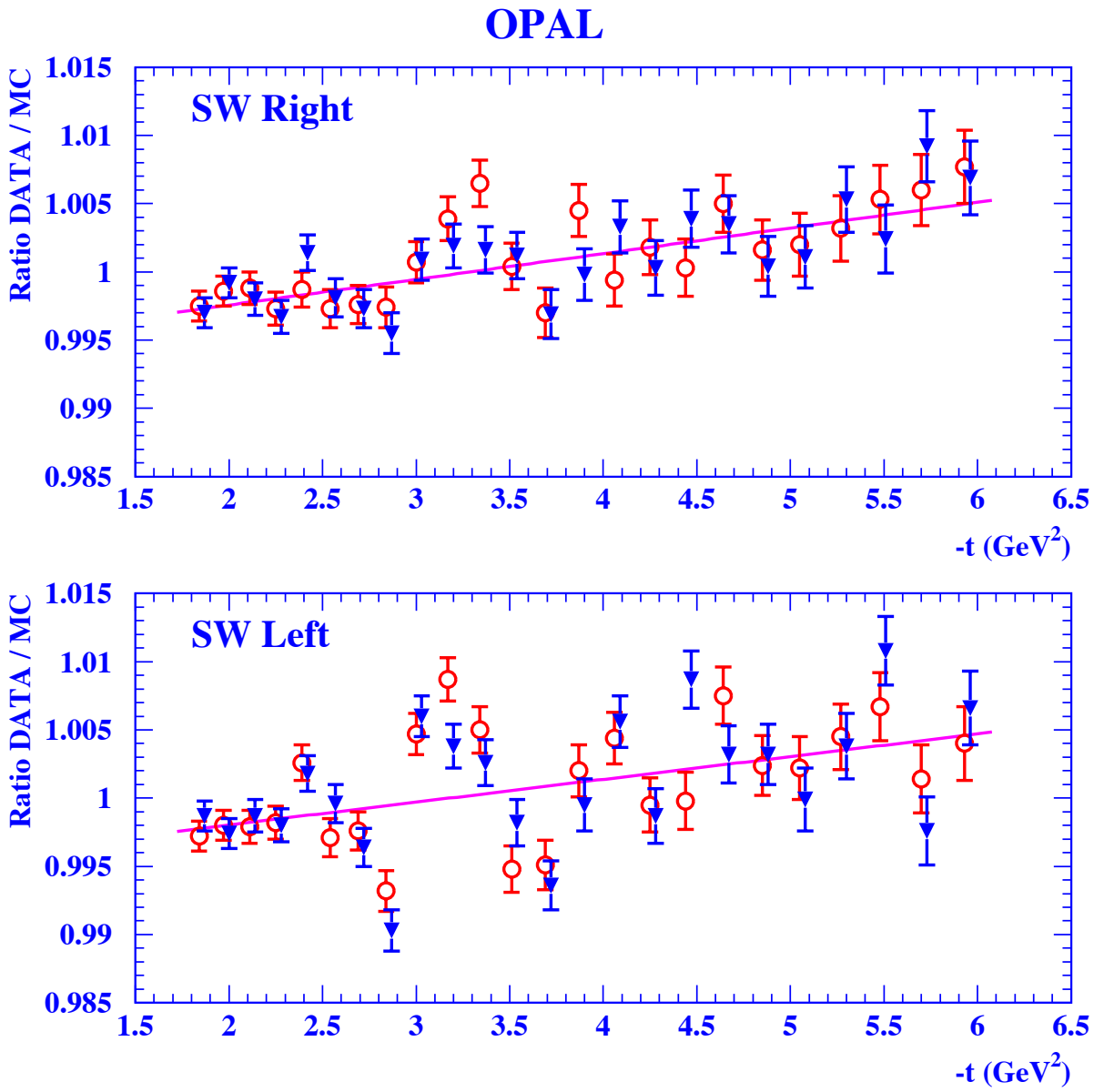

Figure 7: Ratio of data and Monte Carlo (with $\Delta\alpha$ set to zero) for the combination of all LEP1 data, for the Right side (*up*) and the Left side (*bottom*) distributions. Each point corresponds to the size of one radial pad. The solid triangles show the data corrected with anchors in layer 4 X_0, the empty circles the uncorrected data (slightly shifted on the left for clarity), with statistical errors in both cases. The line shows the fit result.

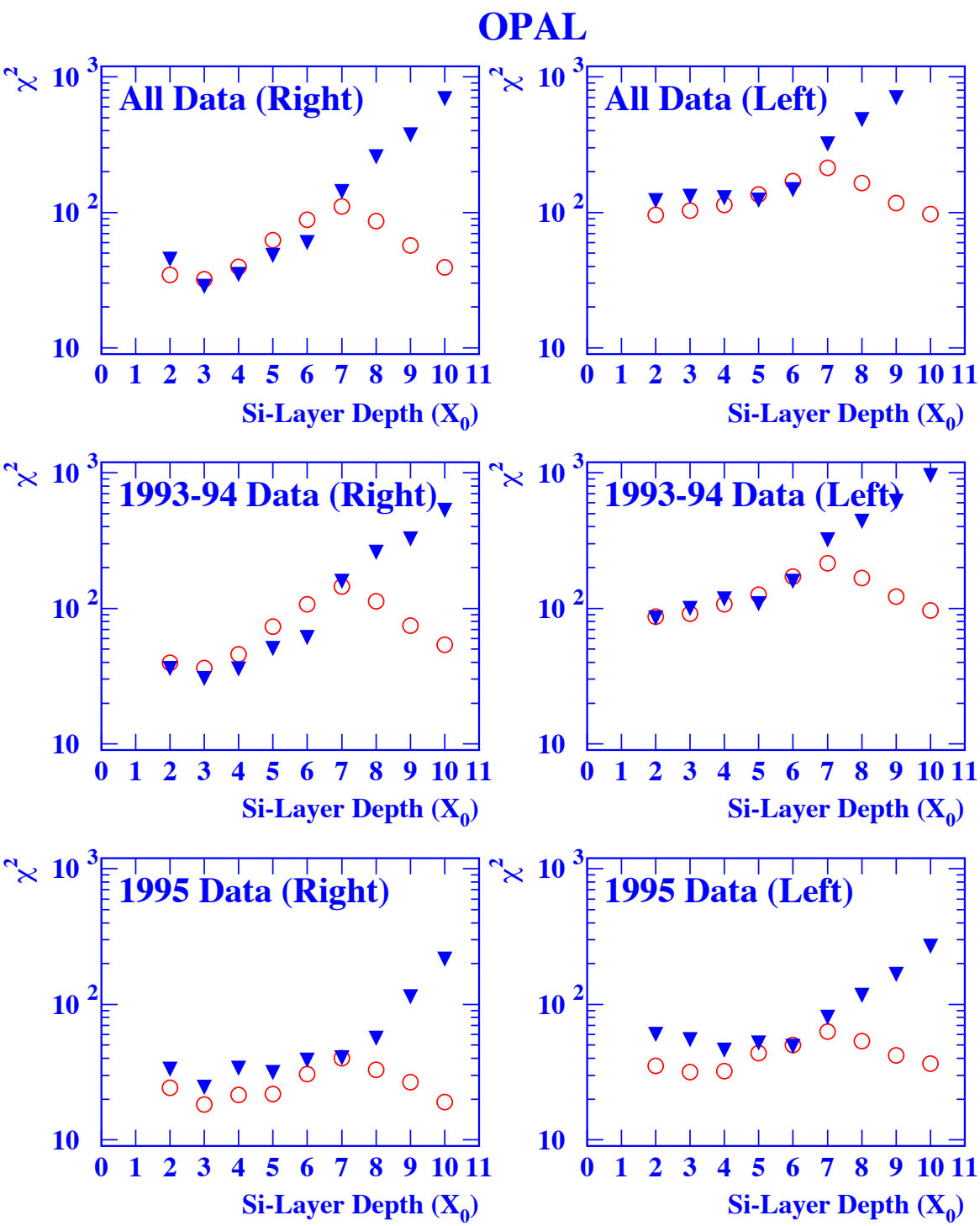

Figure 8: Fit χ^2 (d.o.f.=22) for combined data samples as a function of the anchoring layer, separately for Right and Left distributions. The solid triangles show the χ^2 after anchoring, the open circles for uncorrected distributions. Only statistical errors are considered. The upper plots refer to the combination of all data, the central ones to 1993-94 data, the bottom ones to 1995 data.

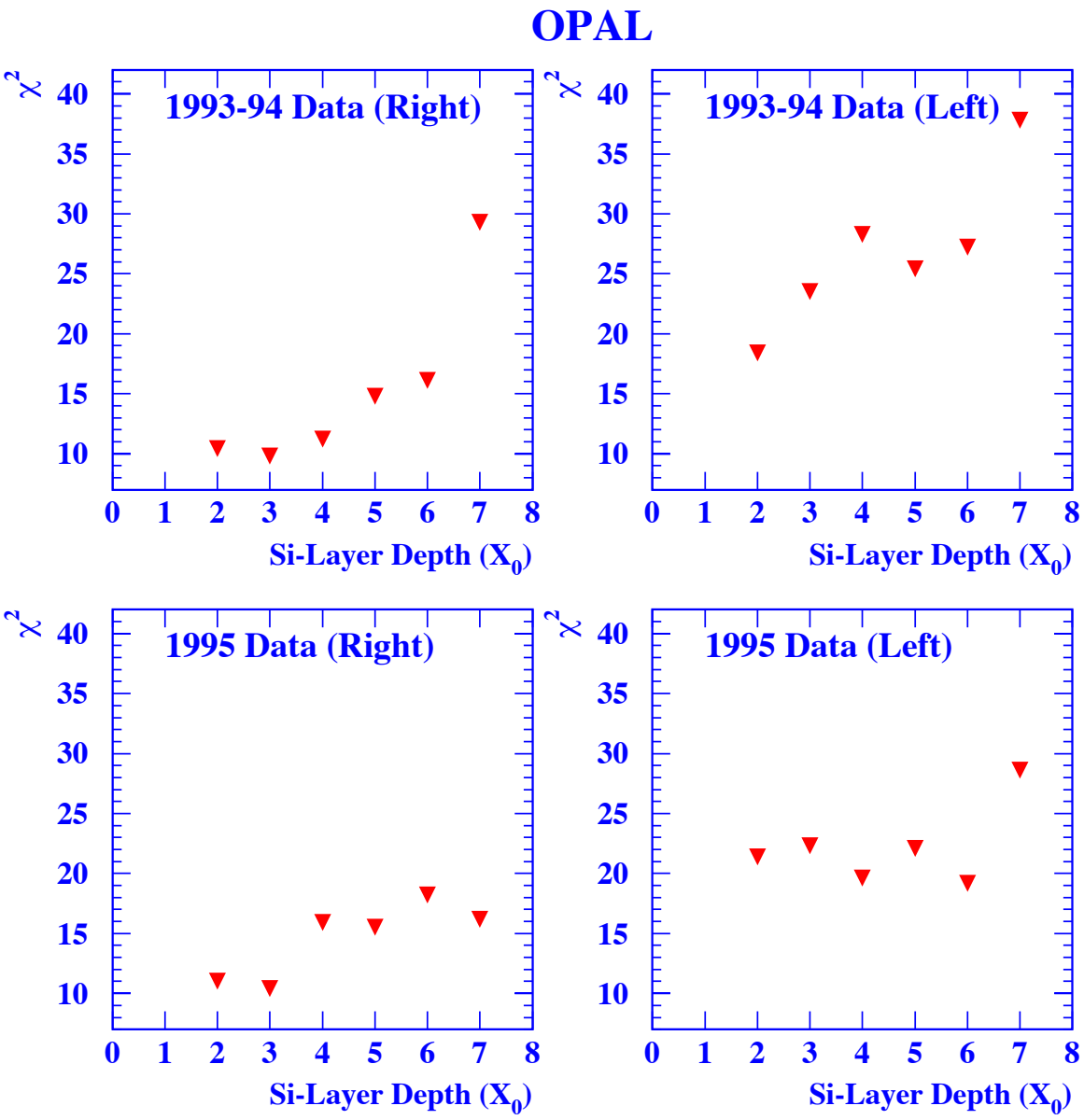

Figure 9: Fit χ^2 (d.o.f.=22) for combined data samples as a function of the anchoring layer, separately for Right and Left distributions. The solid triangles show the χ^2 after anchoring, with statistical and systematic errors described by the covariance matrix. The upper plots refer to the combination of 1993-94 data, the lower ones to 1995 data.

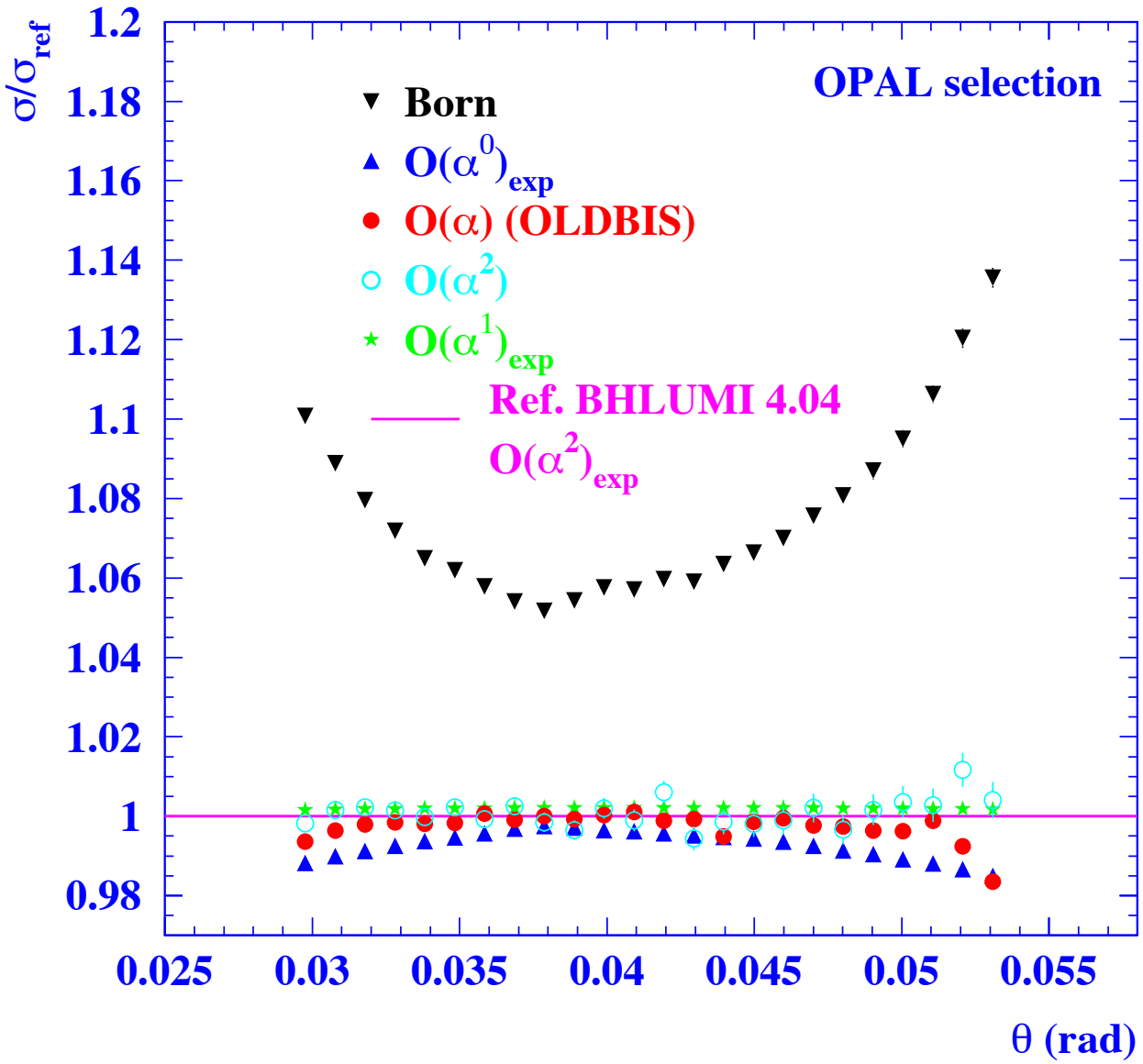

Figure 10: Differential cross section as a function of the polar scattering angle calculated by the BHLUMI package for the OPAL selection in different perturbative approximations, normalized to the reference BHLUMI calculation. Vacuum polarization, Z-interference and s-channel photon contributions are switched off.

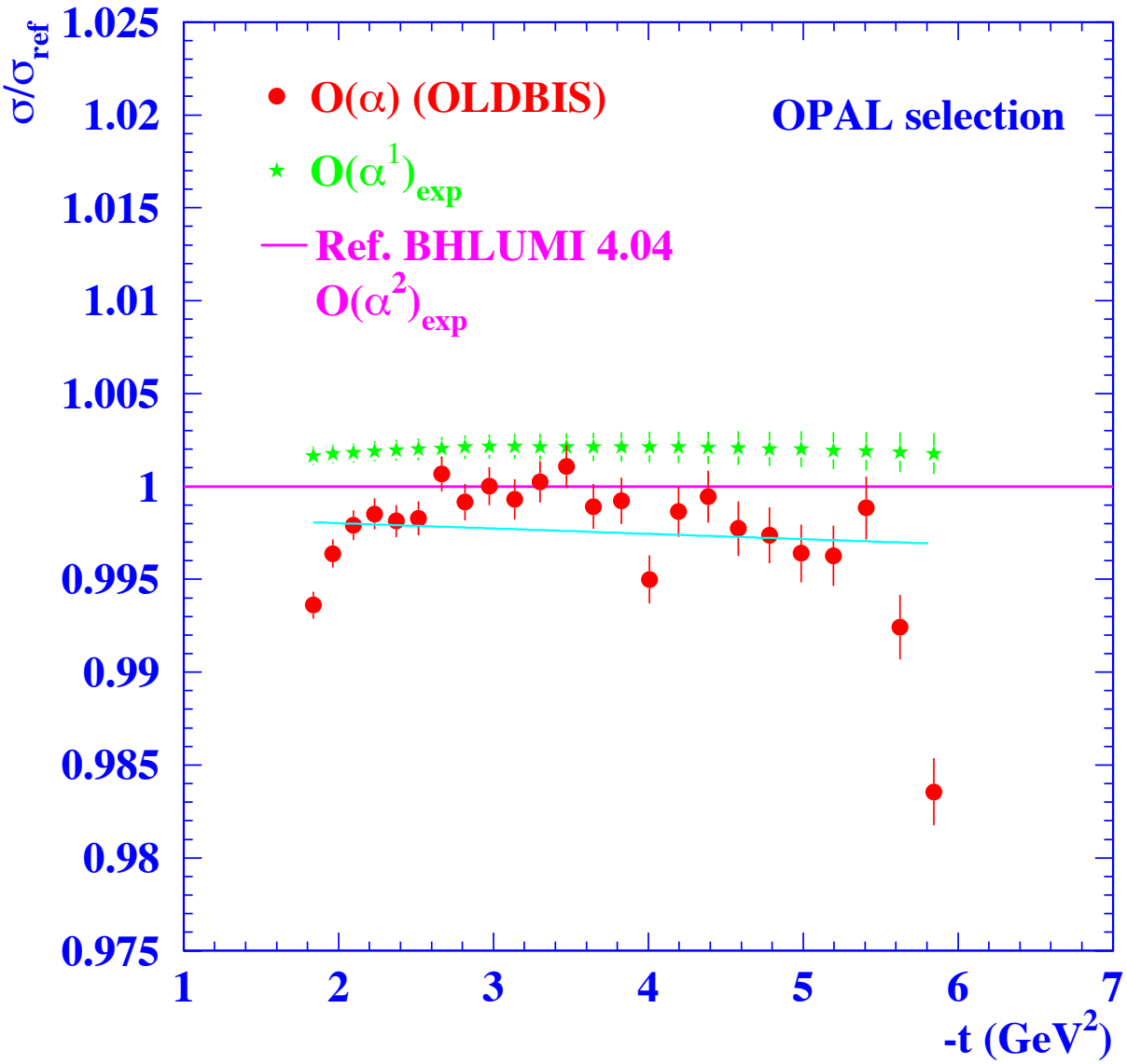

Figure 11: Differential cross section as a function of the polar scattering angle calculated by the BHLUMI package for the OPAL selection with exact (OLDBIS) or exponentiated $\mathcal{O}(\alpha)$ matrix element, normalized to the reference BHLUMI calculation. Vacuum polarization, Z-interference and s-channel photon contributions are switched off. The fitted line is used to conservatively assess the theoretical uncertainty.

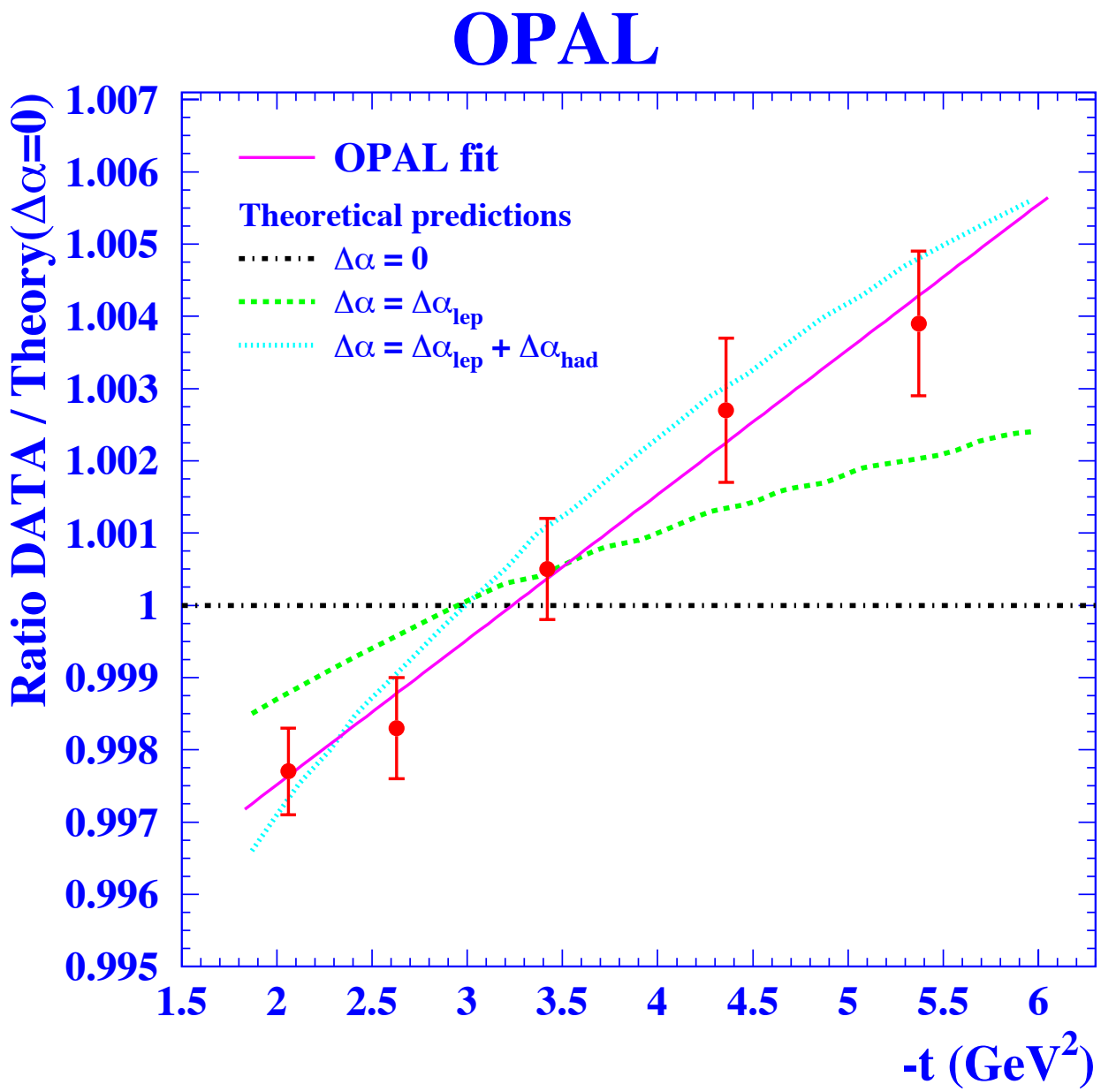

Figure 12: $|t|$ spectrum normalized to the BHLUMI theoretical prediction for a fixed coupling ($\Delta\alpha = 0$). The points show the combined LEP1 data with statistical error bars, the solid line is our fit. The horizontal dot-dashed axis would be the prediction if α were fixed. The dashed curve is the prediction of running α determined by vacuum polarization with only virtual lepton pairs ($\Delta\alpha = \Delta\alpha_{lep}$), the dotted curve with both lepton and quark pairs, calculated by the Burkhardt-Pietrzyk parameterization.